The Astrophysical Journal, 994:249 (19pp), 2025 December 1 https://doi.org/10.3847/1538-4357/ae0e15

JWST Observations of SN 2024ggi. I. Interpretation and Model Comparison of the Type II Supernova 2024ggi at 55 Days past Explosion

E. Baron[1,2], C. Ashall[3,4], J. M. DerKacy[4,5], P. Hoeflich[6], K. Medler[3,4], M. Shahbandeh[5], E. Fereidouni[6], C. M. Pfeffer[3,4,32], T. Mera[6], W. B. Hoogendam[3,32], S. Shiber[6], K. Auchettl[7,8], P. J. Brown[9], C. R. Burns[10], A. Burrow[11], D. A. Coulter[5,12], M. Engesser[5], G. Folatelli[13,14,15], O. Fox[5], L. Galbany[16,17], M. Guolo[12], J. T. Hinkle[3,33], Mark E. Huber[3], E. Y. Hsiao[6], T. de Jaeger[18], D. O. Jones[3], S. Kumar[19], J. Lu[20], P. A. Mazzali[21,22], N. Morrell[23], M. M. Phillips[23], A. Rest[5,12], N. B. Suntzeff[9], B. J. Shappee[3], Jennifer Shi[7], M. D. Stritzinger[24], L. Strolger[5], T. Temim[25], S. Tinyanont[26], M. Tucker[27,28], L. Wang[9], Q. Wang[29], and Y. Yang[30,31]

[1] Planetary Science Institute, 1700 East Fort Lowell Road, Suite 106, Tucson, AZ 85719-2395, USA; ebaron@psi.edu
[2] Hamburger Sternwarte, Gojenbergsweg 112, 21029 Hamburg, Germany
[3] Institute for Astronomy, University of Hawai'i at Manoa, 2680 Woodlawn Drive, Hawai'i, HI 96822, USA
[4] Department of Physics, Virginia Tech, 850 West Campus Drive, Blacksburg, VA 24061, USA
[5] Space Telescope Science Institute, 3700 San Martin Drive, Baltimore, MD 21218-2410, USA
[6] Department of Physics, Florida State University, Tallahassee, FL 32306, USA
[7] School of Physics, The University of Melbourne, VIC 3010, Australia
[8] Department of Astronomy and Astrophysics, University of California, Santa Cruz, CA 95064, USA
[9] George P. and Cynthia Woods Mitchell Institute for Fundamental Physics and Astronomy, Department of Physics and Astronomy, Texas A&M University, College Station, TX 77843, USA
[10] Observatories of the Carnegie Institution for Science, 813 Santa Barbara Street, Pasadena, CA 91101, USA
[11] Homer L. Dodge Department of Physics and Astronomy, University of Oklahoma, 440 W. Brooks, Rm 100, Norman, OK 73019-2061, USA
[12] Physics and Astronomy Department, Johns Hopkins University, Baltimore, MD 21218, USA
[13] Instituto de Astrofísica de La Plata (IALP), CONICET, Paseo del Bosque S/N, B1900FWA La Plata, Argentina
[14] Facultad de Ciencias Astronómicas y Geofísicas Universidad Nacional de La Plata, Paseo del Bosque, B1900FWA, La Plata, Argentina
[15] Kavli Institute for the Physics and Mathematics of the Universe (WPI), The University of Tokyo, Kashiwa, 277-8583 Chiba, Japan
[16] Institute of Space Sciences (ICE, CSIC), Campus UAB, Carrer de Can Magrans, s/n, E-08193 Barcelona, Spain
[17] Institut d'Estudis Espacials de Catalunya (IEEC), E-08034 Barcelona, Spain
[18] LPNHE, (CNRS/IN2P3, Sorbonne Université, Université Paris Cité), Laboratoire de Physique Nucléaire et de Hautes Énergies, 75005, Paris, France
[19] Department of Astronomy, University of Virginia, 530 McCormick Road, Charlottesville, VA 22904, USA
[20] Department of Physics & Astronomy, Michigan State University, East Lansing, MI, USA
[21] Astrophysics Research Institute, Liverpool John Moores University, 146 Brownlow Hill, Liverpool L3 5RF, UK
[22] Max-Planck-Institut für Astrophysik, Karl-Schwarzschild Straße 1, 85748 Garching, Germany
[23] Las Campanas Observatory, Carnegie Observatories, Casilla 601, La Serena, Chile
[24] Department of Physics and Astronomy, Aarhus University, Ny Munkegade 120, DK-8000 Aarhus C, Denmark
[25] Princeton University, 4 Ivy Lane, Princeton, NJ 08544, USA
[26] National Astronomical Research Institute of Thailand, 260 Moo 4, Donkaew, Maerim, Chiang Mai, 50180, Thailand
[27] Center for Cosmology and Astroparticle Physics, The Ohio State University, Columbus, OH, USA
[28] Department of Astronomy, The Ohio State University, Columbus, OH, USA
[29] Department of Physics and Kavli Institute for Astrophysics and Space Research, Massachusetts Institute of Technology, 77 Massachusetts Avenue, Cambridge, MA 02139, USA
[30] Physics Department, Tsinghua University, Beijing, 100084, People's Republic of China
[31] Department of Astronomy, University of California, Berkeley, CA 94720-3411, USA
Received 2025 July 24; revised 2025 September 16; accepted 2025 September 29; published 2025 November 28

Abstract

We present panchromatic 0.4–21 μm observations of the nearby ($\sim$7.2 Mpc) Type II supernova (SN) 2024ggi, obtained during the plateau phase at $\sim$55 days past explosion. Our data set includes JWST spectra spanning 1.7–14 μm, mid-infrared (MIR) imaging at 7.7 and 21 μm, and near-simultaneous ground-based optical and near-infrared (NIR) spectra covering 0.32−1.8 μm. The NIR and MIR spectral features of SN 2024ggi are dominated by H I emission. We present line IDs and a toy PHOENIX/1D model that reproduces the observations well, especially the continuum redward of 0.9 μm. We compare SN 2024ggi to SN 2022acko and SN 2023ixf, two other Type II SNe that were also observed by JWST, and highlight key similarities and differences in their spectral features. No evidence for a MIR excess or dust is found at these epochs, with the model matching the observed flux out to 21 μm. We discuss the model's shortcomings, focusing on the density profile, which

[32] National Science Foundation Graduate Research Fellow.
[33] NASA FINESST Future Investigator.

suppresses line blanketing and produces features in the optical that are too narrow. Our results show the power of panchromatic studies in both exploring the nature of the SN ejecta and constraining detailed models of SNe.

Unified Astronomy Thesaurus concepts: Type II supernovae (1731); Spectroscopy (1558)

1. Introduction

Hydrogen-rich core-collapse supernovae (CC SNe), classified as Type II supernovae (SNe II), mark the deaths of massive stars with initial masses $\gtrsim 8\ M_{\odot}$. These progenitors are typically red supergiants, although exceptions exist, such as the blue supergiant progenitor of SN 1987A (e.g., W. D. Arnett et al. 1989). Binary evolution likely plays a significant role in shaping the final evolutionary state of the progenitor. Massive stars—at the end of their lives—form degenerate iron cores, which, upon exceeding the Chandrasekhar mass, undergo gravitational collapse to nuclear densities. This process releases ∼100 foe of energy (1 foe $= 10^{51}$ erg; G. E. Brown 2005), primarily in the form of neutrinos, but also powers the optical supernova (SN) display. The explosion is inherently aspherical, and fully modeling the collapse and explosion remains computationally challenging. As such, the detailed mechanisms driving core collapse and the resulting observable signatures remain active areas of research (e.g., H.-T. Janka 2025; D. Vartanyan et al. 2025).

To date, the number of panchromatic optical-to-mid-infrared (MIR) observations of SNe II is limited, because much of the wavelength regime is not observable from the ground. Yet, the near-infrared (NIR) and MIR contain a wealth of information because lines are less blended and more varied compared to the optical and ultraviolet. The lower optical depths in the NIR and MIR also reveal the inner ejecta at earlier times (W. P. S. Meikle et al. 1993) and at later times can contain signatures of both molecule and dust formation (J. Spyromilio et al. 1988, 2001; D. H. Wooden et al. 1993; J. Rho et al. 2018).

Infrared (IR) observations of CC SNe were pioneered with the explosion of SN 1987A (P. Bouchet et al. 1987, 1991; E. Oliva et al. 1987; R. M. Catchpole et al. 1988, 1989; J. H. Elias et al. 1988; D. M. Rank et al. 1988; P. A. Whitelock et al. 1988; W. P. S. Meikle et al. 1989, 1991, 1993; C. M. Sharp & P. Hoeflich 1990; I. J. Danziger et al. 1991). These studies demonstrated the wealth of information available at these wavelengths and laid the groundwork for the interpretation of future IR observations. SN 1987A continues to be studied in the NIR and MIR with the James Webb Space Telescope (JWST; O. C. Jones et al. 2023; J. Larsson et al. 2023).

Since SN 1987A, many SNe II have been observed using ground-based NIR (1–2 μm) resources allowing the characterization of spectral line evolution from a couple of days past the explosion through the nebular phase (S. Benetti et al. 2001; M. Hamuy et al. 2001; A. Elmhamdi et al. 2003; M. Pozzo et al. 2006; A. Pastorello et al. 2009; K. Maguire et al. 2010; M. Fraser et al. 2011; L. Tomasella et al. 2013; M. Dall'Ora et al. 2014; A. Jerkstrand et al. 2014; T. Morokuma et al. 2014; K. Takáts et al. 2014, 2015; S. Valenti et al. 2015, 2016; J. Rho et al. 2018; K. A. Bostroem et al. 2019; T. Szalai et al. 2019; M. A. Tucker et al. 2024). For example, SN 1999em was well observed with NIR spectroscopy, providing line identifications and additional analysis (M. Hamuy et al. 2001; A. Elmhamdi et al. 2003). S. Davis et al. (2019) presented the results of 30 SNe II with 81 NIR spectra obtained by the Carnegie Supernova Project 2 (E. Y. Hsiao et al. 2019; M. M. Phillips et al. 2019) and were able to discern correlations between the strength of the He I lines and the formation of CO. However, at wavelengths longer than 2 μm, there is still a dearth of data.

The era of MIR spectroscopy ($\lambda > 2\ \mu$m) for CC SNe began to take traction with the launch of the Spitzer Space Telescope (SST) with observations of SNe 2004et, 2004dj, and 2005af (R. Kotak et al. 2009; O. D. Fox et al. 2011; T. Szalai & J. Vinkó 2013), which showed the evolution of CO, and dust in the ejecta. However, these data sets did not have continuous wavelength coverage from the optical to MIR and hence lacked complete coverage of key spectral features such as the CO fundamental band at ∼4 μm.

More recently, a number of CC SNe have been observed with JWST, including the SNe II 2022acko (M. Shahbandeh et al. 2024) and 2023ixf (J. M. DerKacy et al. 2025; K. Medler et al. 2025a). The launch of JWST opened the window to continuous spectral coverage into the MIR, allowing the construction of panchromatic multiepoch optical-to-MIR data sets of SNe. Observations of SN 2022acko at ∼50 days show many series of H lines and a lack of preexisting molecules or dust (M. Shahbandeh et al. 2024), revealing the promise that the construction of these data sets offers. SNe II are heterogeneous at optical wavelengths (K. R. Hinds et al. 2025), due to variations in both the progenitor systems and explosion processes. IR observations probe deeper into the ejecta than optical photons, opening a new window into the ejecta structure.

SN 2024ggi was discovered by the Asteroid Terrestrial-impact Last Alert System (S. Srivastav et al. 2024; J. Tonry et al. 2024; T.-W. Chen et al. 2025) on 2024 April 11 (MJD 60411.14) in the host galaxy NGC 3621 located at a distance of 7.24 ± 0.20 Mpc (A. Saha et al. 2006)—making SN 2024ggi, along with SN 2023ixf, one of the closest SNe in modern times. The transient was classified as an SN II with flash ionization features (W. Hoogendam et al. 2024; Q. Zhai et al. 2024). Due to the proximity of SN 2024ggi and its early discovery, JWST Director Discretionary Time was approved to observe it throughout its evolution through program JWST-GO-6677/6716 (PI: Ashall; C. Ashall et al. 2024a, 2024b).[34] The purpose of this program is to follow the NIR and MIR spectroscopic evolution of SN 2024ggi from the plateau phase to ∼300 days past explosion.

We present the first epoch of these observations, which were obtained ∼55 days post explosion. In addition to the spectra and photometry obtained with JWST, optical and NIR spectra were obtained with Spectroscopic Classification of Astronomical Transients (SCAT) program (M. A. Tucker et al. 2022) and the Hawaii Infrared Supernova Study (HISS; K. Medler et al. 2025b), respectively. The features in the observed spectra are identified. We present non-LTE (NLTE) `PHOENIX` models that reproduce the features and continuum in NIR and MIR and discuss their shortcomings.

[34] https://chrisashall.com/mid-infrared-supernova-collaboration-mirsnac/

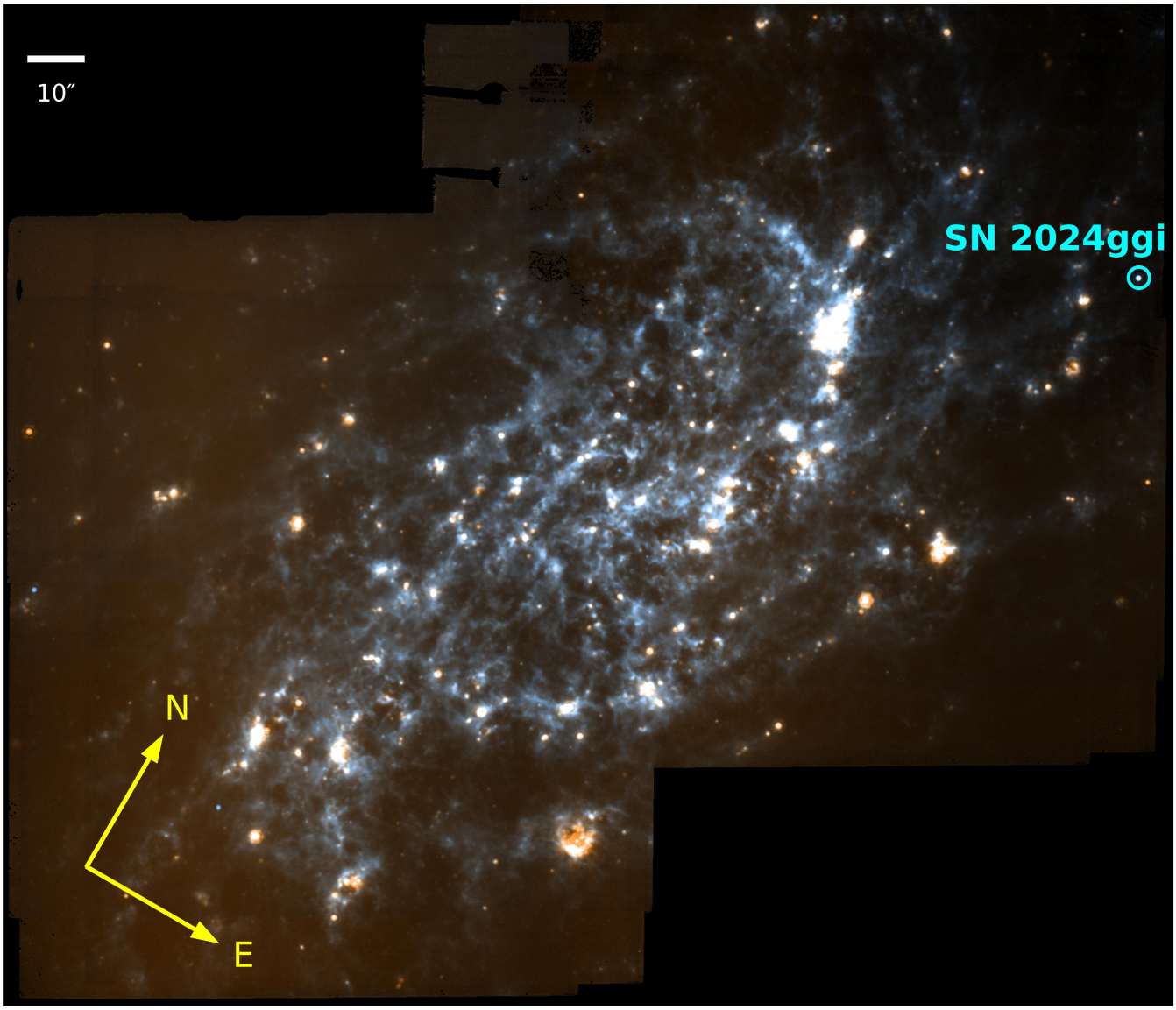

Figure 1. A composite two-band color image constructed from the MIRI imaging of NGC 3621 using filters F700W and F2100W. The location of SN 2024ggi is highlighted with the turquoise circle.

1.1. Previous Work

While we focus on our panchromatic observations at one epoch on the plateau, SN 2024ggi has been well observed at early times. Here, we briefly review the previous work on SN 2024ggi.

High-resolution spectra of SN 2024ggi were obtained with the MIKE spectrograph on the Magellan Clay Telescope 21, 27, 28, and 34 hr after discovery (T. Pessi et al. 2024; M. Shrestha et al. 2024). They show solid evidence of flash ionization features. The early spectra were compared to detailed radiative-transfer models, and a mass-loss rate of $\dot{M} = 4 \times 10^{-3} M_{\odot}\,\mathrm{yr}^{-1}$ was inferred (M. Shrestha et al. 2024). Thus, there is evidence for interaction of the ejecta with the surrounding circumstellar medium (CSM).

Early-time (+8 to +17 days) observations using Atacama Large Millimeter/submillimeter Array (ALMA) millimeter data (M. Hu et al. 2025) and high-cadence optical spectroscopy (T. Pessi et al. 2024; J. Zhang et al. 2024) have been crucial in probing the CSM around the progenitor. While

Table 1
Basic Observational Parameters of SN 2024ggi Used in This Work

Parameter	Value	Source
R.A. (hh:mm:ss)	11:18:22.087	(1, 2)
Decl. (deg:arcmin:arsec)	−32:50:15.27	(1, 2)
$T_{\rm exp}$ (MJD)	60410.80 ± 0.34	(3)
$M_{V_{\rm max}}$ (mag)	∼−17.72	(4)
z	0.002435	(5)
Distance (Mpc)	7.24 ± 0.20	(5)
μ (Mpc)	29.30 ± 0.03	(5)
$E(B-V)_{\rm MW}$ (mag)	0.054 ± 0.02	(4, 6)
$E(B-V)_{\rm Host}$ (mag)	0.034 ± 0.02	(5)
$E(B-V)_{\rm Cloud}$ (mag)	0.066 ± 0.02	(4)
Host	NGC 3621	(1)

References. (1) TNS (https://www.wis-tns.org/object/2024ggi), (2) K. C. Chambers et al. (2024), (3) W. V. Jacobson-Galán et al. (2024), (4) M. Shrestha et al. (2024), (5) A. Saha et al. (2006), (6) E. F. Schlafly & D. P. Finkbeiner (2011).

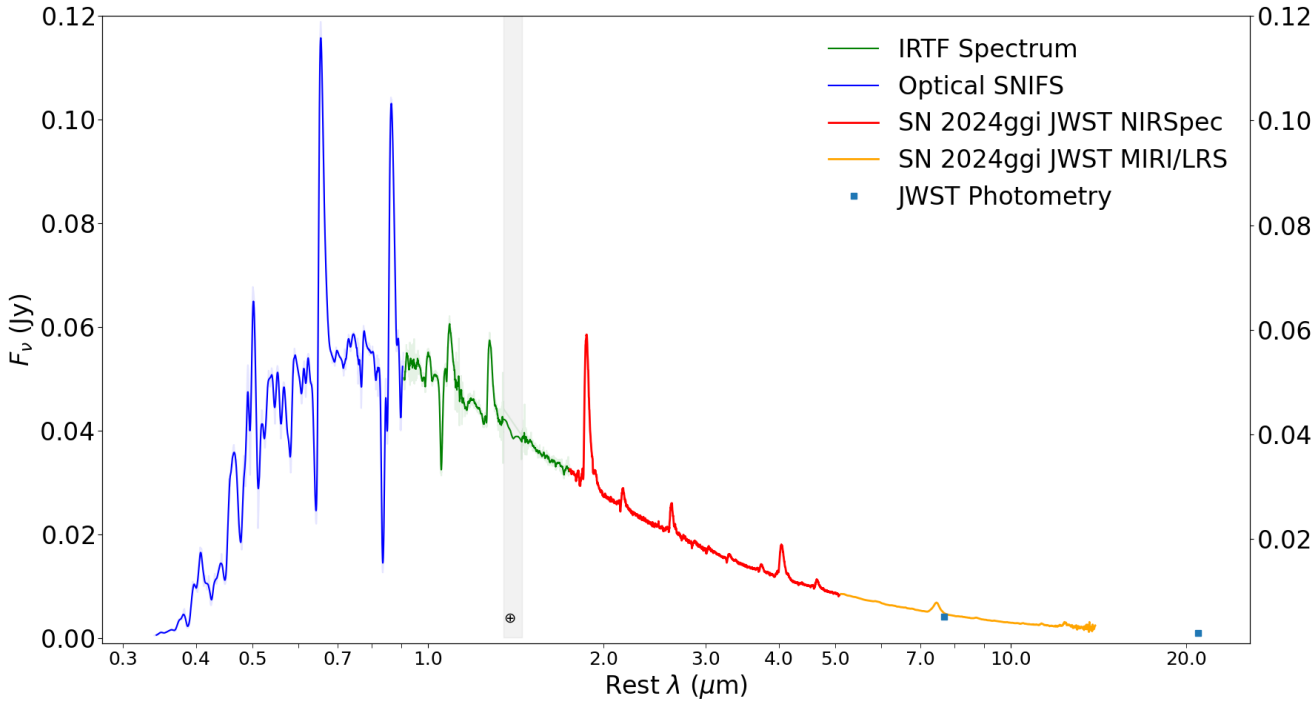

Figure 2. The full dereddened SED of SN 2024ggi. The UH88 optical spectrum was obtained on MJD 60470 (day ∼ 60); the IRTF spectrum was obtained on day 44. The NIRSpec spectrum was obtained on MJD 60466.46 (day 55), and the MIRI/LRS spectrum was obtained in the same visit as the NIRSpec. We note that the F700W and F2100W images were taken ∼9 days after the JWST spectra, which might explain the flux discrepancy between the photometry and the spectra.

Table 2
The Photometry Obtained with JWST

Filter	Obs. Date (MJD)	Exp. Time (s)	Phase (days)	Magnitude (mag)
F770W	60474.7995	44	63.84	14.885 ± 0.002
F2100W	60474.864	172	63.91	16.443 ± 0.017

ALMA did not detect emission, the results help distinguish between a steady wind and an eruptive mass-loss scenario, with an eruptive model favored and a derived mass-loss rate of approximately $5 \times 10^{-3}\,M_\odot\,\mathrm{yr}^{-1}$ (M. Hu et al. 2025). Early light curves are well described by a broken power law with a break at ∼1 day (M. Shrestha et al. 2024). Flash ionization features indicate CSM velocities of ∼20–40 km s^{-1}, radii of $3-6 \times 10^{14}$ cm, and mass-loss rates ranging from 10^{-3} to $10^{-1}\,M_\odot\,\mathrm{yr}^{-1}$ (W. V. Jacobson-Galán et al. 2024; M. Shrestha et al. 2024; J. Zhang et al. 2024; T.-W. Chen et al. 2025).

The CSM mass is estimated at $0.4\,M_\odot$ (T.-W. Chen et al. 2025), and the maximum observed velocities reach up to 8000 km s^{-1} (J. Zhang et al. 2024). Spectroscopic observations within the first 2 days postdiscovery reveal flash ionization features of H I, He I, He II, C III, C IV, N III, and Si IV (T. Pessi et al. 2024; T.-W. Chen et al. 2025). The line profiles are best fit with Voigt profiles, and the broad emission components increase in velocity over time, suggesting an accelerated, radiatively driven wind (T. Pessi et al. 2024). Notably, high-ionization lines such as He II are sometimes absent (J. Zhang et al. 2024). Comparisons to CMFGEN (D. J. Hillier & D. L. Miller 1998) and other detailed models reproduce the ionization state at ∼1 day and the blue edge of Hα at ∼15 days, but no model fits all features perfectly (W. V. Jacobson-Galán et al. 2024; J. Zhang et al. 2024).

Light-curve modeling, including the rapid early blueward evolution and the presence of flash ionization features, supports a scenario involving wind shock breakout (T.-W. Chen et al. 2025). Explosion energies are inferred to be 2×10^{51} erg, with ejecta masses of $1.2\,M_\odot$ and CSM radii of $4-6 \times 10^{14}$ cm (X. Chen et al. 2024; W. V. Jacobson-Galán et al. 2024; J. Zhang et al. 2024; T.-W. Chen et al. 2025). The derived mass-loss rates and CSM masses are difficult to reconcile with steady-state wind mass loss (N. Smith 2017) or standard neutrino-driven core-collapse explosion mechanisms (N. Soker 2024).

Progenitor properties have been constrained using preexplosion imaging from the Hubble Space Telescope, the SST, and the Dark Energy Camera Legacy Survey (X. Chen et al. 2024; D. Xiang et al. 2024). The progenitor is identified as a variable star consistent with a red supergiant, with a mass-loss rate of less than $3 \times 10^{-6}\,M_\odot\,\mathrm{yr}^{-1}$ prior to the enhanced mass-loss phase inferred from the flash ionization (D. Xiang et al. 2024). This result is corroborated by light-curve and spectral modeling that finds that the CSM distribution likely consists of a two-component structure with a compact core and extended tail (K. Ertini et al. 2025). K. Ertini et al. (2025) find the progenitor fits a zero-age main $M_{\mathrm{ZAMS}} = 15\,M_\odot$, with a pre-SN mass $14.1\,M_\odot$ and a mass-loss rate of $4 \times 10^{-3}\,M_\odot\,\mathrm{yr}^{-1}$, giving an explosion energy 1.3 foe. Analysis of the progenitor environment indicates a uniform spatial distribution and a star formation history corresponding to a progenitor mass of $10.2\,M_\odot$ (X. Hong et al. 2024). Semianalytic modeling and archival imaging yield ejecta masses of $1.2\,M_\odot$, a progenitor radius of $555\,R_\odot$, and progenitor masses in the range $14–17\,M_\odot$ (X. Chen et al. 2024).

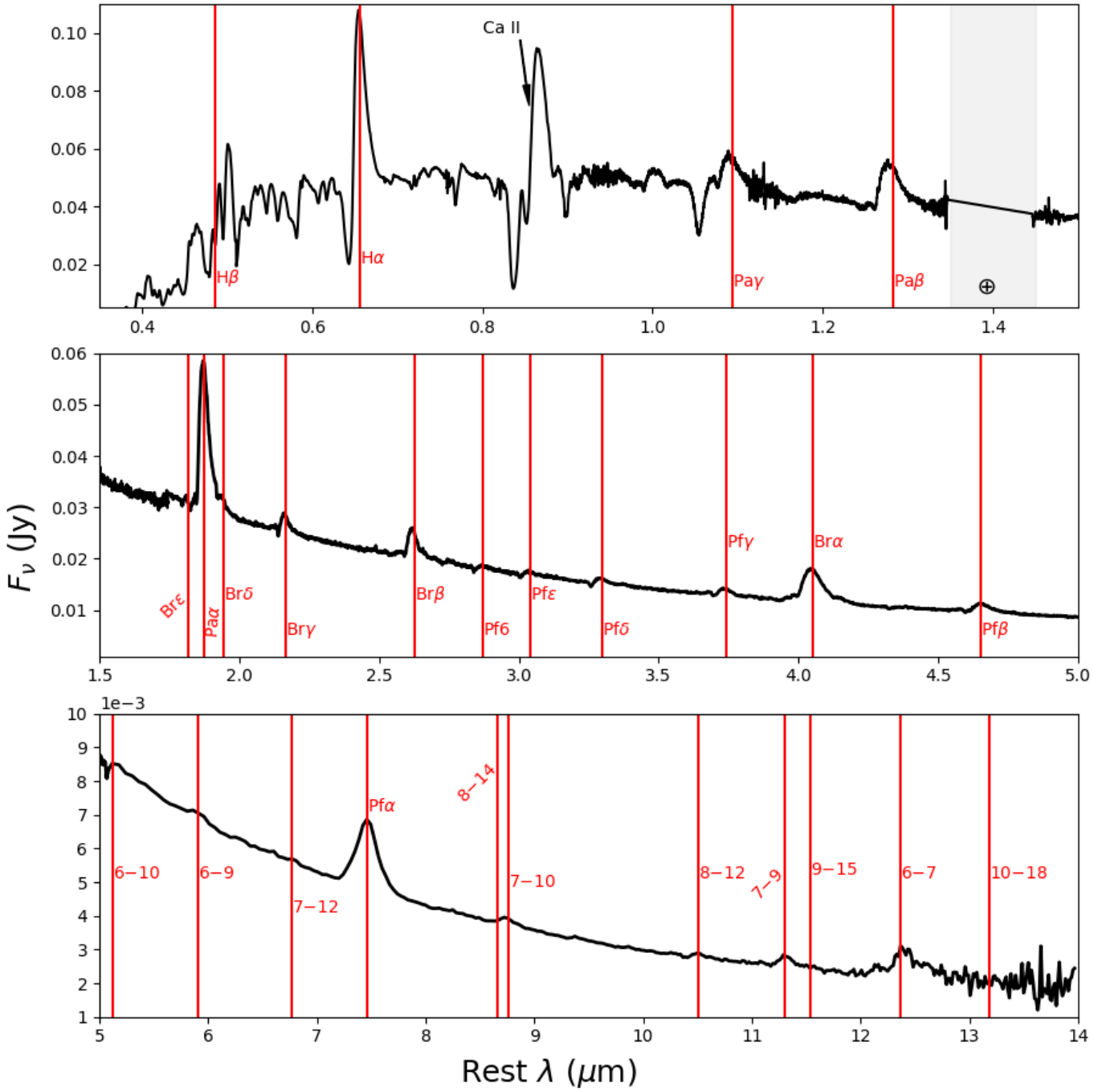

Figure 3. The optical, ground-based NIR, and JWST SN 2024ggi spectra with prominent H I lines identified.

2. Observations and Data Reduction

The basic parameters we use throughout this work are presented in Table 1. We take the time of first light from W. V. Jacobson-Galán et al. (2024): MJD 60410.80 ± 0.34 days, which is based on the average between the times of the last nondetection and first detection. (Unless stated otherwise, we will quote epochs in time since first light, referring interchangeably to this as time since explosion). We adopt the total extinction estimate of $E(B-V)_{\rm total} = 0.154$ mag (M. Shrestha et al. 2024), which is similar to values found in other investigations (W. V. Jacobson-Galán et al. 2024; T. Pessi et al. 2024). We note that in addition to extinction in the host and the Galaxy, M. Shrestha et al. (2024) include extinction from an intervening cloud at redshift $z = 0.00039$ and that their extinction estimates rely on the Na D equivalent width formula of D. Poznanski et al. (2012), which is known to have a large error (M. M. Phillips et al. 2013).

2.1. JWST Spectra

Spectroscopic observations were obtained at ∼55 days past explosion using the fixed slit with the NIRSpec and the Mid-Infrared Instrument (MIRI) Low Resolution Spectrometer (LRS). This produced continuous spectral data from ∼1.6 to 14 μm. The resolving power of these observations is ∼1000 for NIRSpec and ∼100 for MIRI/LRS. All data were reduced using the JWST pipeline version 1.18.0 and CRDS context

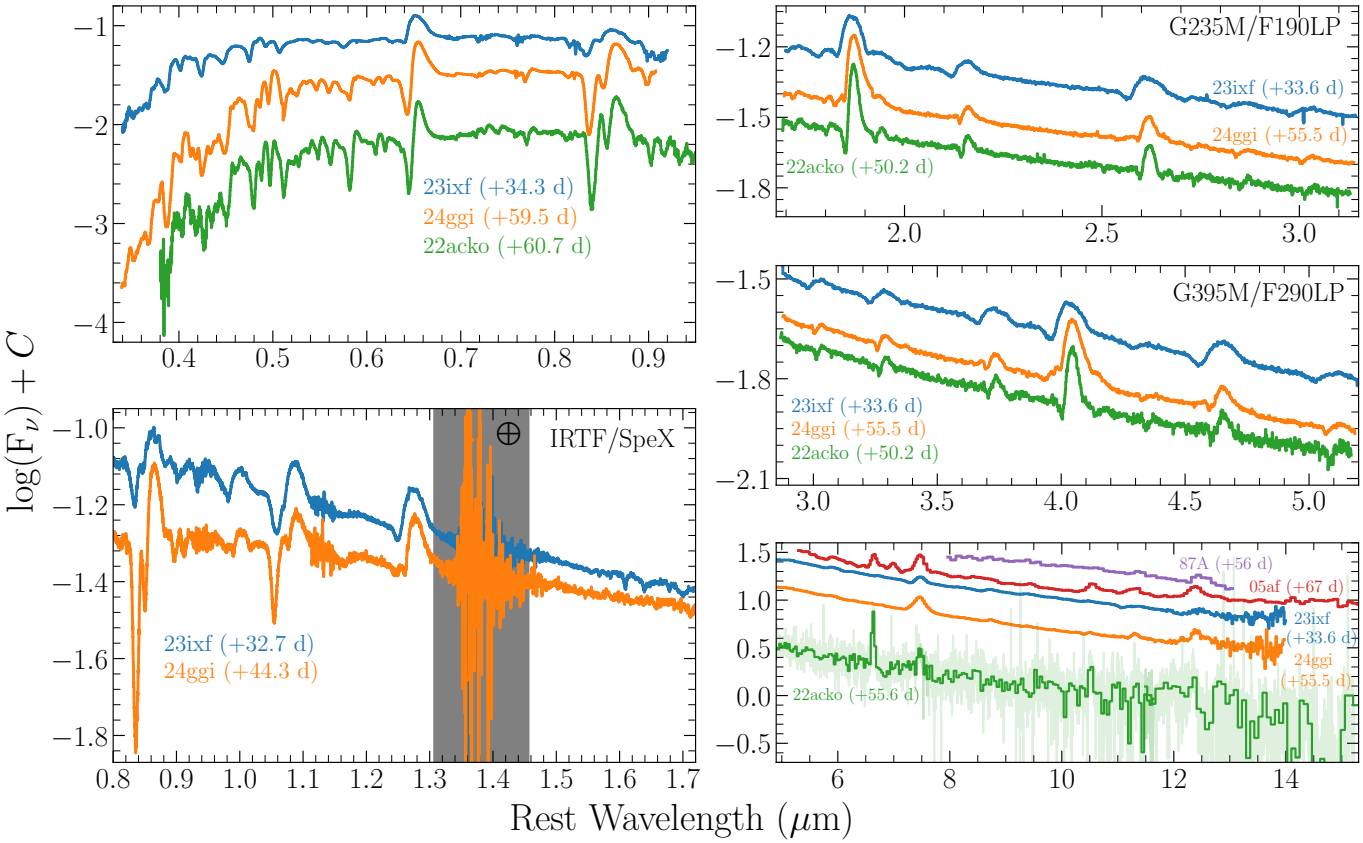

Figure 4. Panchromatic spectral comparison of SNe II observed with JWST (SNe 2022acko, 2023ixf, and 2024ggi) during the plateau phase and other historical SNe II (SNe 1987A D. K. Aitken et al. 1988) and (SN 2005af R. Kotak et al. 2006) observed in the MIR at similar phases. The SN 2022acko data shown here have been re-reduced using updated versions of the JWST pipeline (v1.18.0+`jwst_1371.pmap` and v1.17.1+`jwst_1363.pmap` for the NIRSpec and MIRI/MRS data, respectively) relative to the data first presented in M. Shahbandeh et al. (2024).

`jwst_1371.pmap`. A log of the spectral observations can be found in Table A1.

2.2. JWST Imaging

The Physics at High Angular Resolution in Nearby Galaxies collaboration (J. C. Lee et al. 2022; A. Leroy et al. 2023) obtained serendipitous imaging of SN 2024ggi in the JWST MIRI filters F770W and F2100W at ∼64 days. As SN 2024ggi was located at the edge of the field of view, it is only visible in two of the four dithers in each of these filters. Figure 1 presents a color composite of SN 2024ggi and the host galaxy NGC 3621.

Point-spread function (PSF) photometry was computed using a custom-made Python notebook making use of the *WebbPSF* photometry package (M. D. Perrin et al. 2014).[35] The PSF width was determined by minimizing the residual while also taking into account the secular increase of the PSF with wavelength. The fluxes of each dither, where the SN was visible, were averaged, and the error in the flux was obtained using the standard deviation of the fluxes. A log of the photometric observations is presented in Table 2.

2.3. Ground-based Spectra

In order to fill out the spectral energy distribution (SED), we obtained optical and NIR spectra at a similar epoch to the JWST data. An optical (0.32–0.9 μm) spectrum was obtained as part of the SCAT program (M. A. Tucker et al. 2022), using the SuperNova Integral Field Spectrograph (SNIFS; B. Lantz et al. 2004) mounted on the University of Hawaii 88 inch telescope. The data were obtained 59.5 days (MJD = 60470.27) past explosion with a 1200 s exposure and reduced using the procedure outlined in M. A. Tucker et al. (2022).

To observe the NIR, we also obtained a NASA Infrared Telescope Facility (IRTF) spectrum (Program 2024A987, PI: Hoogendam) 44.43 days (MJD = 60455.23) past explosion as part of HISS (K. Medler et al. 2025b). The IRTF spectrum had an exposure time of 1434.5 s, consisting of 12 A/B individual 119.5 s exposures and was reduced using the methods described by the HISS team (W. B. Hoogendam et al. 2025a, 2025b; K. Medler et al. 2025b).

The SNIFS spectra are not processed with the full SNFactory pipeline and are thus not spectrophotometric; however, only minor (roughly 10%) adjustments in flux were needed to match the IRTF spectrum to that of JWST, which was then matched to the SNIFS spectrum again with minor adjustments. We focus on the flux-calibrated JWST spectra for the spectral modeling.

3. Data Analysis

3.1. SED

Figure 2 shows the full 0.32–20 μm SED of SN 2024ggi at ∼55 days past explosion. The spectra are consistent with a recombination-dominated regime characterized by numerous hydrogen line transitions. Despite the ground-based and JWST

[35] https://github.com/orifox/psf_phot/blob/main/space_phot/MIRI/miri_1028.ipynb

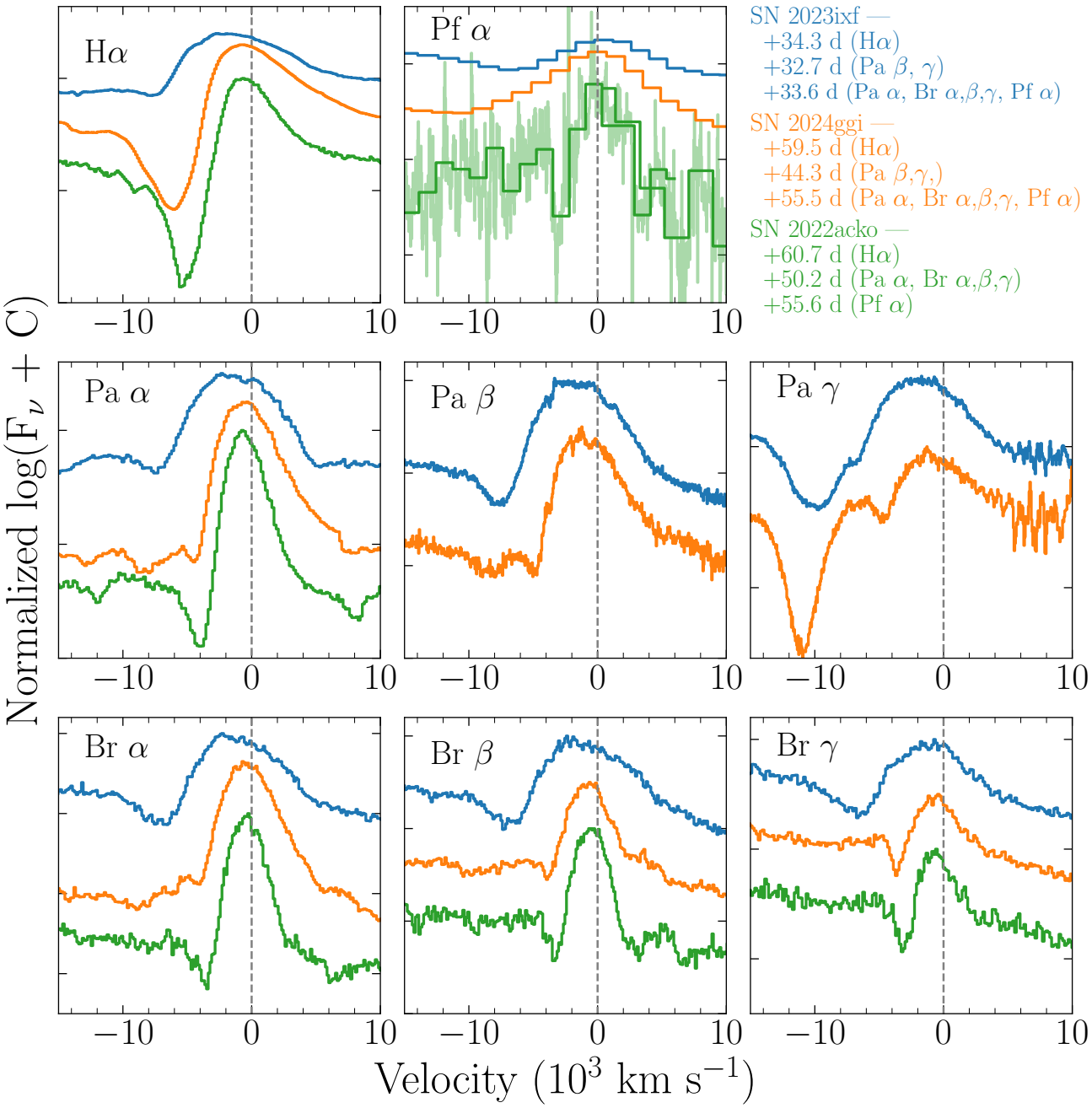

Figure 5. A velocity-space comparison of some strong P-Cygni profiles found in JWST and ground-based observations of SNe 2022acko, 2023ixf, and 2024ggi.

spectra being obtained at a slightly different phase, they align in flux with only modest matching. The photometric data, which were taken ∼9 days after the JWST data, have a flux slightly below that of the spectra.

Figure 3 shows that, except for the optical wavelengths, all of the major features in both the IRTF and the JWST spectra are accounted for by lines of H I. The strength and width of these lines reflect transitions within the atomic structure, with the strongest features arising from the most probable or lowest-energy level transitions.

3.2. Spectral Comparison

Both SN 2022acko (M. Shahbandeh et al. 2024) and SN 2023ixf (J. M. DerKacy et al. 2025) have panchromatic data sets (near-) contemporaneous with their JWST observations during the plateau phase. These comparisons are shown in Figure 4. JWST data were obtained approximately at the midpoint of the plateau phase for each SN. We note that the spectra of SN 2022acko used in the figure have been re-reduced using the `AstroBkgInterp`[36] package, which recovers the SN continuum better than the reduction presented by M. Shahbandeh et al. (2024).

In general, all three SNe show features typical of normal SNe II on the plateau. In the optical, the later observation epoch of SN 2022acko and SN 2024ggi compared to that of SN 2023ixf results in stronger blanketing by iron-group lines

[36] https://github.com/brynickson/AstroBkgInterp

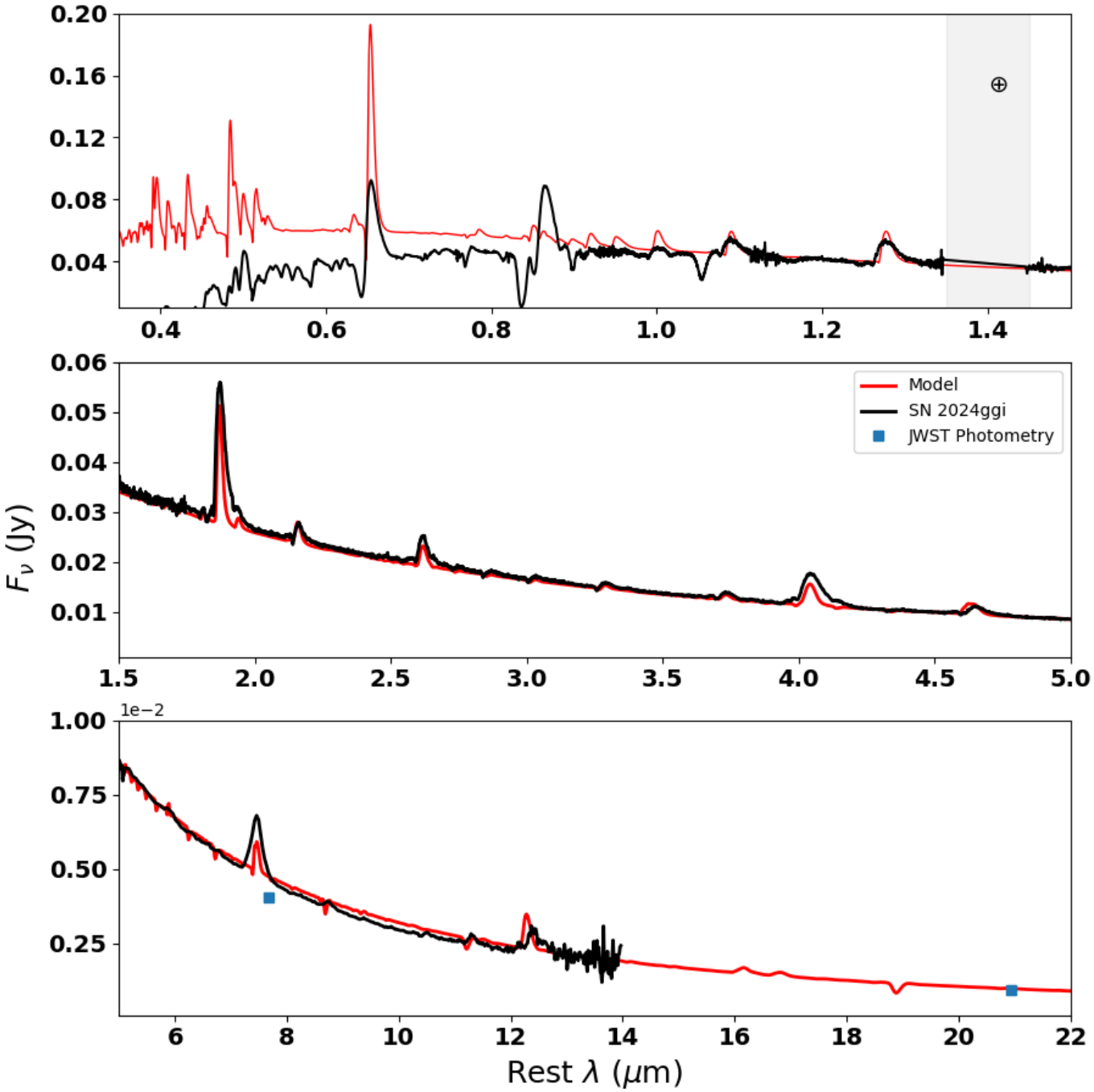

Figure 6. The observed day 55 SN 2024ggi ground-based and JWST spectra compared to the PHOENIX model (see Section 4.2). In this and subsequent model plots, the synthetic spectrum has been scaled to the observed spectrum at 3 μm.

in the blue optical wavelengths and more *s*-process lines observed. While J. M. DerKacy et al. (2025) identify the He I 1.083 μm line in the ground-based IRTF spectra of SN 2023ixf, we see no strong evidence for lines of He I in SN 2024ggi. The lower velocity of the Paschen lines in SN 2024ggi results in less blending than is seen in SN 2023ixf. The feature blueward of Paγ is more likely due to the C I 1.069 μm line than to the He I 1.083 μm line (see Section 5).

In the JWST/NIRSpec observations, there is near uniformity among all three objects in the H lines that are present in the spectrum. At MIR wavelengths ($\lambda > 5\,\mu$m), all three SNe are dominated by hydrogen lines of the Pfund, Humphreys, and unnamed higher-order series. The emission peaks of the strong Pfα plus Huβ blend and the Huα line are more prominent in SN 2024ggi, similar to SN 2005af, than in SNe 1987A or 2023ixf. The lower signal-to-noise ratio of the SN 2022acko data makes distinguishing all but the strongest hydrogen lines difficult.

3.3. Spectral Line Velocities

More detailed comparisons focusing on the hydrogen lines with strong P-Cygni features in the three JWST SNe II (e.g., Hα; Pa α, β, γ; Br α, β, γ; and Pfα) are shown in Figure 5. Though the

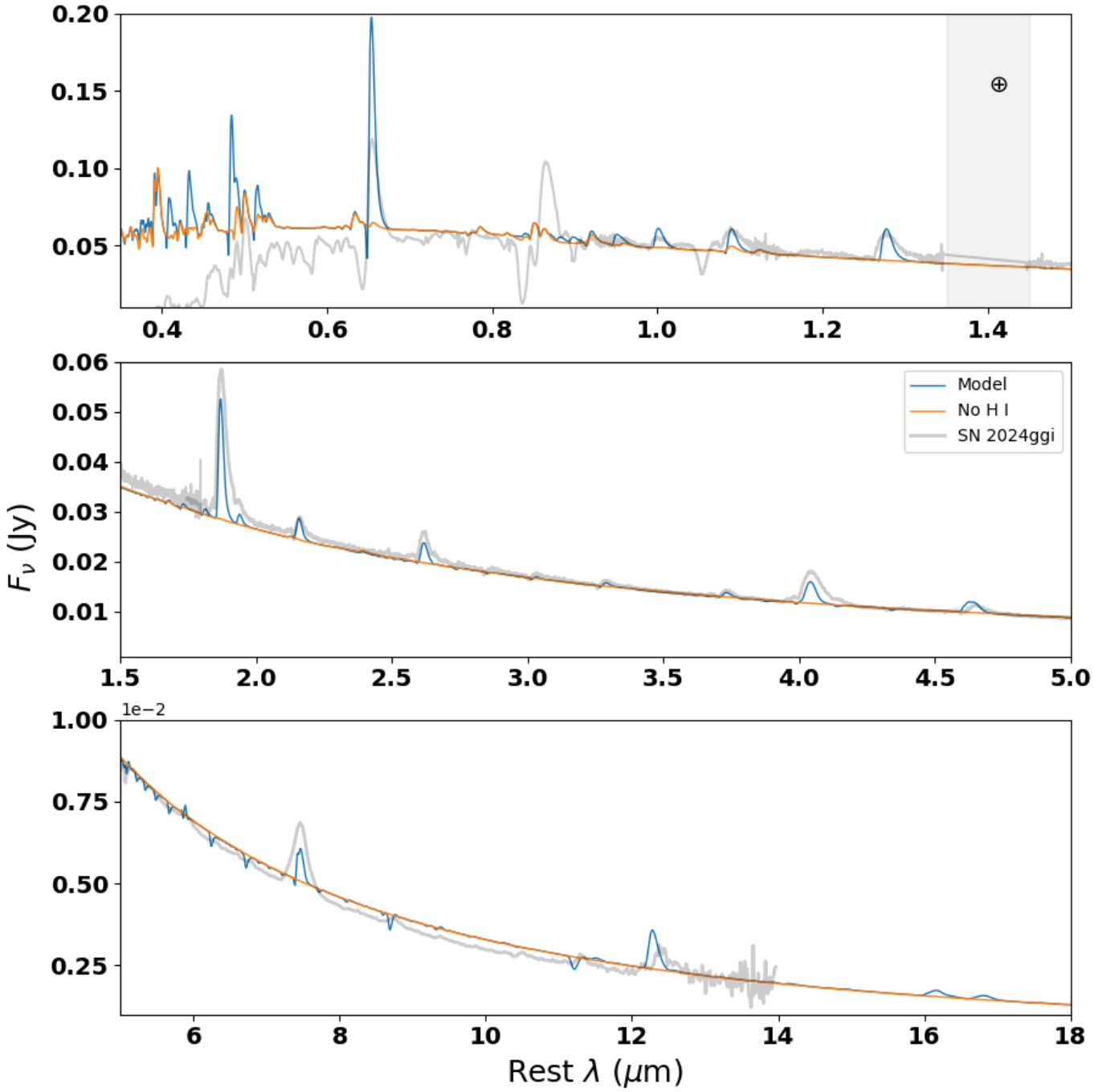

Figure 7. The observed day 55 SN 2024ggi JWST spectrum, the PHOENIX model, and the PHOENIX model with all H I lines turned off. Most of the observed spectral features are due to H I lines.

phases of the SNe with respect to explosion vary somewhat, the wide variation in the line shapes gives an indication of the degree of heterogeneity of the SN IIP subclass. One trend that is homogeneous across all three SNe is the correlation between line velocity (measured from the P-Cygni absorption trough) and the absolute V-band magnitude (M. Hamuy & P. A. Pinto 2002; T. de Jaeger et al. 2020). SN 2022acko has $M_V \sim -15.4$ mag (K. A. Bostroem et al. 2023), while SN 2023ixf has $M_V \sim -18.2$ mag (W. Zheng et al. 2025), and SN 2024ggi has $M_V \sim -17.7$ mag (Table 1). As Figure 5 shows, this trend is consistent across multiple series of H lines, not just the Hβ and Fe II λ5169 lines commonly used as characteristic measures of the photospheric velocity in SNe II.

Not only are the line profiles heterogeneous across the SN II sample but also within each SN. Unlike SN 2023ixf, which shows multiple examples of substructure within the H lines (A. Singh et al. 2024; J. M. DerKacy et al. 2025), SN 2024ggi shows no substructures common to multiple H series, at this phase. The closest thing to substructure seen in SN 2024ggi is a small peak at ~ -1300 km s^{-1} in the Paschen β, γ, δ, and ζ lines. The feature may be present in other lines, but it is too weak to be distinguished given the line profile variability.

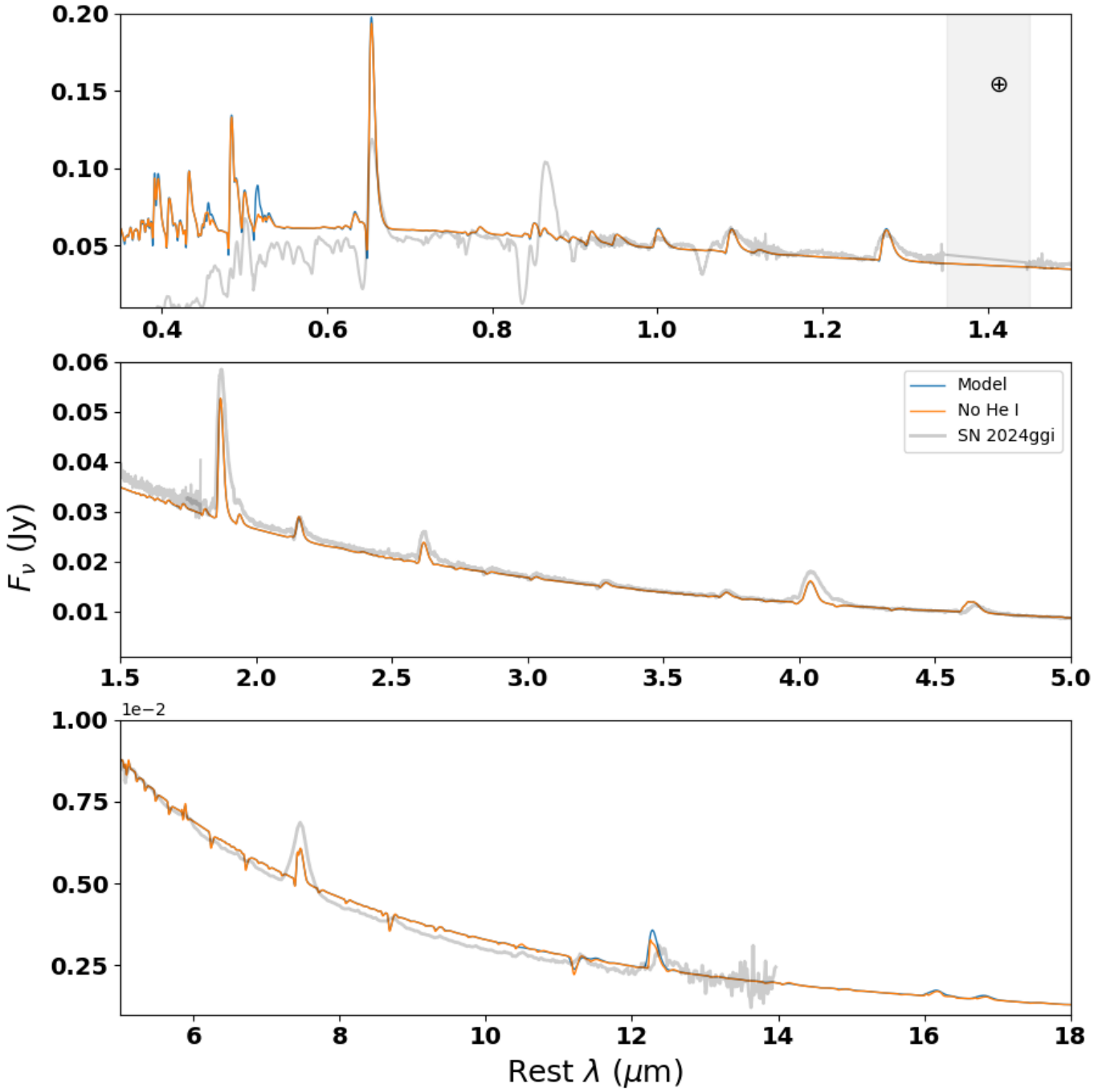

Figure 8. The observed day 55 SN 2024ggi ground-based and JWST spectrum, the PHOENIX model, and the PHOENIX model with all He I lines turned off. The one He I line that is prominent in the model spectrum is nearly coincident with the Huα line. Thus, there is no strong evidence for He I lines at this epoch and observed wavelength range.

4. Models

Synthetic spectral models of CC SNe have a long history (C. Payne-Gaposchkin & F. L. Whipple 1940; D. Branch 1980), but the advent of SN 1987A prompted much work (R. P. Harkness & J. C. Wheeler 1988; P. Hoeflich 1988; L. B. Lucy 1988; R. G. Eastman & R. P. Kirshner 1989; D. A. Swartz et al. 1989; P. A. Mazzali et al. 1992; P. H. Hauschildt & L. M. Ensman 1994; C. Kozma & C. Fransson 1998; R. C. Mitchell et al. 2002). Numerical approaches roughly fall into three classes: (i) Direct modeling approaches such as that used by the SYNOW code (D. J. Jeffery & D. Branch 1990); (ii) grid-based solution of the radiative-transfer equation, such as PHOENIX/1D (P. H. Hauschildt & E. Baron 1999), HYDRA (P. Hoeflich 1988), and CMFGEN (D. J. Hillier & D. L. Miller 1998; L. Dessart & D. J. Hillier 2005); and (iii) Monte Carlo methods such as those of Mazzali (P. A. Mazzali et al. 1992), ARTIS (S. A. Sim 2007; M. Kromer & S. A. Sim 2009), TARDIS (W. E. Kerzendorf & S. A. Sim 2014), SEDONA (D. Kasen et al. 2006), and SUMO (A. Jerkstrand et al. 2011).

Here we use SYNOW and PHOENIX/1D. SYNOW generates synthetic SN spectra by modeling the photospheric phase with a few simplifying assumptions: spherical symmetry and

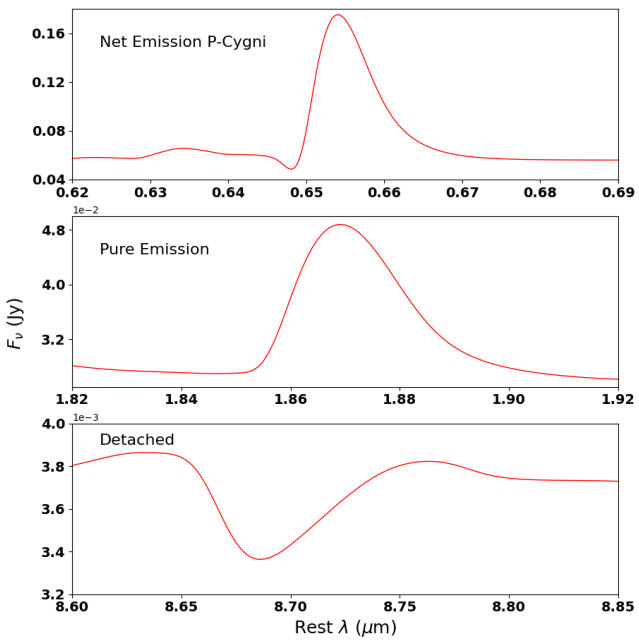

Figure 9. The three different line types seen in the models. Top panel: the strongly net-emission P-Cygni Hα line. Middle panel: a nearly pure emission line (transition). Bottom panel: a P-Cygni line that appears to be pure absorption in Figure 6. The line is essentially detached (see Section 4.3).

homologous expansion; and a sharp photosphere emitting a blackbody continuum with only line transport that is treated as resonance scattering in the Sobolev approximation ignoring ionization and rate equations. The output is a blackbody continuum overlaid with blended P-Cygni profiles. We only focus on Hα here, but in general, for each ion, the input parameters are the Sobolev optical depth of a reference line photospheric velocity ($v_{\rm phot}$) and the e-folding velocity of the reference line optical depth, v_e. Optical depths decline exponentially with velocity: $\tau(v) = \tau(v_{\rm phot})\exp[-(v - v_{\rm phot})/v_e]$. See D. J. Jeffery & D. Branch (1990) and D. Branch et al. (2005, 2006) for more details.

PHOENIX/1D is a generalized stellar atmosphere code that solves the radiative-transfer equation along characteristic rays in spherical symmetry, fully accounting for special-relativistic effects. It treats NLTE rate equations for a comprehensive set of ions. Primary NLTE transitions determine level populations and opacity; weaker lines are added in LTE using the NLTE ground-state occupation, ensuring no transition is omitted. Energy balance is enforced in the comoving frame, implicitly incorporating time-dependent effects through PdV work and gamma-ray deposition. The outer boundary sets the observer-frame bolometric luminosity; the inner boundary condition is set by requiring that the flux at the deepest zone is determined by the diffusion approximation, evaluated at that boundary.

PHOENIX/1D has been used on a wide variety of SNe including SN 1993J (E. Baron et al. 1993, 1995), SN 1994I (E. Baron et al. 1996, 1999), SN 1998S (E. J. Lentz et al. 2001c), SN 1999em (E. Baron et al. 2000, 2004), SN 1987A (R. C. Mitchell et al. 2002), SN 1993W (E. Baron et al. 2003), and SNe Ia (P. Nugent et al. 1995; E. J. Lentz et al. 2001a, 2001b; E. Baron et al. 2006, 2008; S. Bongard et al. 2006, 2008; B. Friesen et al. 2017; J. M. DerKacy et al. 2020).

4.1. Methods

Given that both the ground-based and JWST spectra are dominated by H I lines (Section 3), we model the spectra to place constraints on the line formation processes in the ejecta. The goal is to produce a model that matches the overall spectra and not to tweak the model to match every single feature. Thus, using the generalized stellar atmospheres code PHOENIX (P. H. Hauschildt & E. Baron 1999), we constructed a simple model assuming a power-law density profile, $\rho \propto v^{-n}$, with $n = 13$ and $v_{\rm max} = 5900$ km s^{-1}. The model has solar abundances (M. Asplund et al. 2009). The low outer velocity is intended to mimic the effect of circumstellar interaction. The luminosity is $L = 2 \times 10^9\, L_\odot$, the ejecta mass (mass exterior to $\tau_{\rm std} = 10$, where $\tau_{\rm std}$ is the optical depth in the continuum at 5000 Å) is $M_{\rm ejecta} = 9.1\, M_\odot$, with kinetic energy $E_{\rm ejecta} = 0.48$ foe. Since the spectra were dominated by hydrogen recombination lines, we were able to choose rather generic parameters for SNe IIP (based on previous studies) and thus, did not need to vary our initial parameter choices, except for the outer pressure (which determines $v_{\rm max}$) in order to obtain the fiducial model.

4.2. Results

Figure 6 shows the fiducial model described above (Section 4.1) compared to the data from the optical to the MIR. While the JWST spectra were obtained at 55 days, the optical UH88 spectrum is at ∼60 days and the IRTF spectrum is at ∼44 days; the model is constructed at 55 days. The model does a very good job of fitting the NIR+MIR continuum ($\lambda > 0.9\,\mu$m). However, the relatively steep density profile significantly inhibits line blanketing in the UV, showing that the true ejecta density profile is not captured by a single power law.

Our goal is not to produce a perfect fit to the full data set, but rather, we focus on the fit associated with the NIR+MIR data, and thus, we take this model as our fiducial model.

Figure 7 shows the fiducial model (blue) and the same model with the H I opacities turned off (orange). Beyond the Ca IR triplet (0.757789, 0.758322, and 0.760342 μm), there are hardly any observed features not accounted for by H I lines.

Figure 8 shows the fiducial model (blue) and the same model with the He I opacities turned off (orange). The only strong features are the singlet and triplet transitions near 0.50 μm and the singlet and triplet transitions near 12.2 μm.

The only neutral helium lines clearly evident in Figure 8 are the 1S-1P λ5017.1 line and the 3P-3D multiplet near 12.26 μm, but the presence of Huα at 12.372 μm makes that identification weak. There are a few other features that contribute somewhat blueward of 0.5 μm. It is possible that the feature just blueward of Paγ is due to the He I 1.083 μm line, but the C I 1.069 μm line seems to be a more likely identification (see Section 5). Thus, the entire observed spectrum is well explained solely by lines of neutral hydrogen.

4.3. Line Profiles

An obvious inconsistency of the model is that it does not reproduce the strong observed high-velocity component seen in the Ca IR triplet (and possibly the Mg II 0.9226 μm line) in the optical+NIR (from the spectrum obtained on the IRTF),

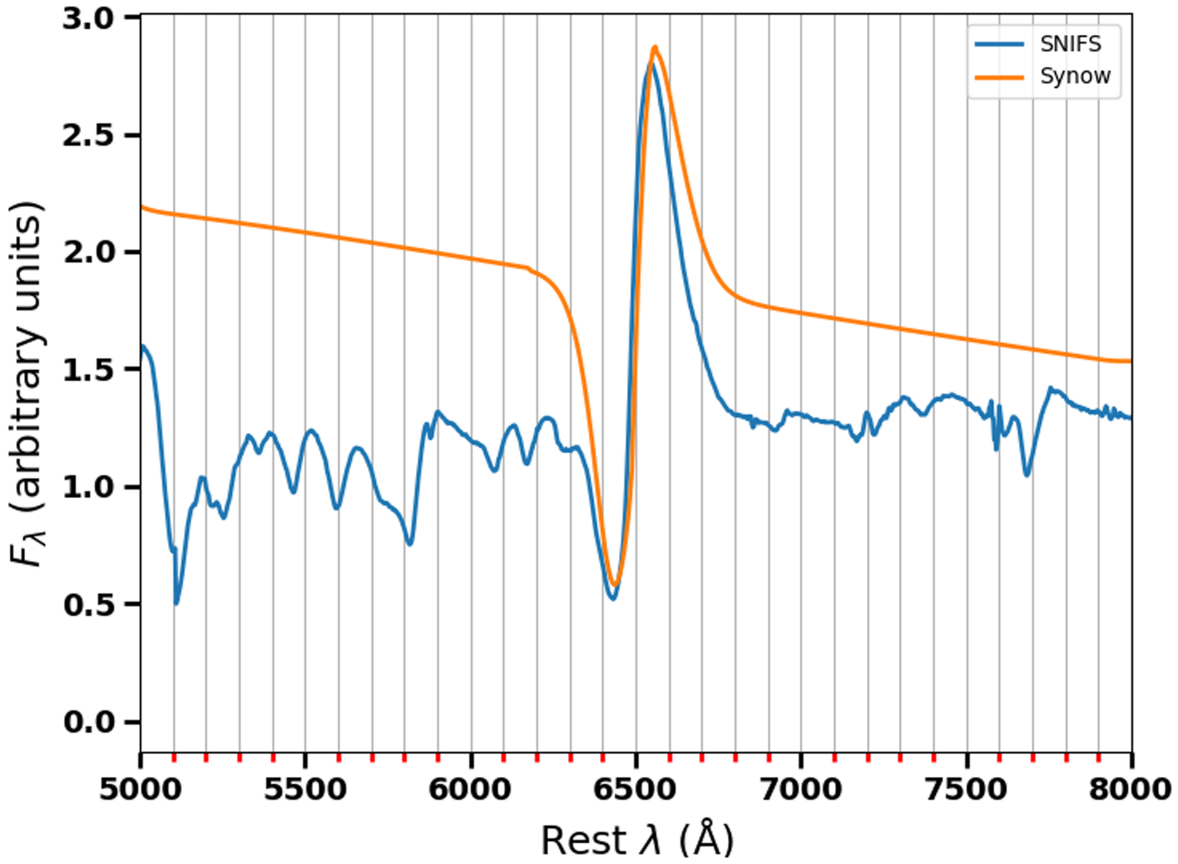

Figure 10. A SYNOW fit to the Hα line in SN 2024ggi. The optical depth is $\tau = 10$, $v_{\rm phot} = 3500$ km s^{-1}, the density profile is given by an exponential with $v_e = 2000$ km s^{-1}, and $v_{\rm max} = 20{,}000$ km s^{-1}.

but this is inherent in the model since the atmosphere contains no material at velocities above 5900 km s^{-1}. While the model does an excellent job of fitting the JWST line profiles blueward of 5 μm and redward of 5 μm, the model predicts absorption profiles where the observations show emission profiles. Although the Pfα line is not a great fit in the model, it does show strong net emission as observed. However, for the 7–10 H I feature at 8.76 μm, the observations show net emission, while the model shows a nearly pure absorption line. This is likely due to a lack of significant optical depth in the line at the photosphere but significant optical depth in the line above the photosphere (such that the line is "detached"; see, for example, D. Branch et al. 2003). In the fiducial model, $v_{\rm phot} = 3000$ km s^{-1}. (In PHOENIX models, there is no predefined photosphere, so $v_{\rm phot}$ is *not* defined a priori, as it is in SYNOW. In PHOENIX, we therefore define $v_{\rm phot}$ as the point where $\tau_{\rm std} = 1$). Examining the departure coefficients shows that the Pfα levels are both underpopulated, whereas levels 7 and 10 are quite overpopulated to the model surface, making the line likely to be detached.

Figure 9 shows the three different line types produced by the model (and seen in the observations): strongly net-emission P-Cygni (Hα), a nearly pure emission line, and a P-Cygni line that appears strongly in absorption. The latter corresponds to a detached feature.

The PHOENIX/1D model does a relatively poor job of fitting the blue absorption troughs of the H I optical lines, even while fitting the line widths in the NIR and MIR. In this work, we are focused on using a simple toy model that describes the NIR + MIR. However, it is worth examining the velocity extent of Hα. Figure 10 shows a SYNOW calculation of Hα, which does a relatively good job of fitting the velocity extent of the feature.

The SYNOW parameters are $\tau = 10$ and $v_{\rm phot} = 3500$ km s^{-1}; the density profile is given by an exponential with $v_e = 2000$ km s^{-1}, and $v_{\rm max} = 20{,}000$ km s^{-1}. This density profile is significantly shallower than the PHOENIX/1D model, leading to the more extended blue absorption trough in the P-Cygni line profile.

4.4. Velocity Extent

Although there are no indications of molecular or dust emission at this early phase, it is useful to know the velocity extent of the ejecta in order to constrain the emission radius for future dust. We have run several models in addition to the fiducial model to explore this. Unfortunately, simply extending the velocity extent without altering the density profile does not affect the predicted spectrum significantly enough to draw conclusions about whether the ejecta could extend to higher velocity. Figure 11 shows the fiducial model and a model with $v_{\rm max} = 12{,}250$ km s^{-1}.

5. Discussion

The observations and modeling show that, with the exception of the Ca IR triplet and the C I 1.069 μm line, all the features in the NIR+MIR spectrum can be attributed to H I. Figure 12 shows the velocity extent of the Paγ line (left) and the C I 1.069 μm line (right). They both have roughly the same velocity ($\sim$4800 km s^{-1} for Paγ and $\sim$4300 km s^{-1} for C I).

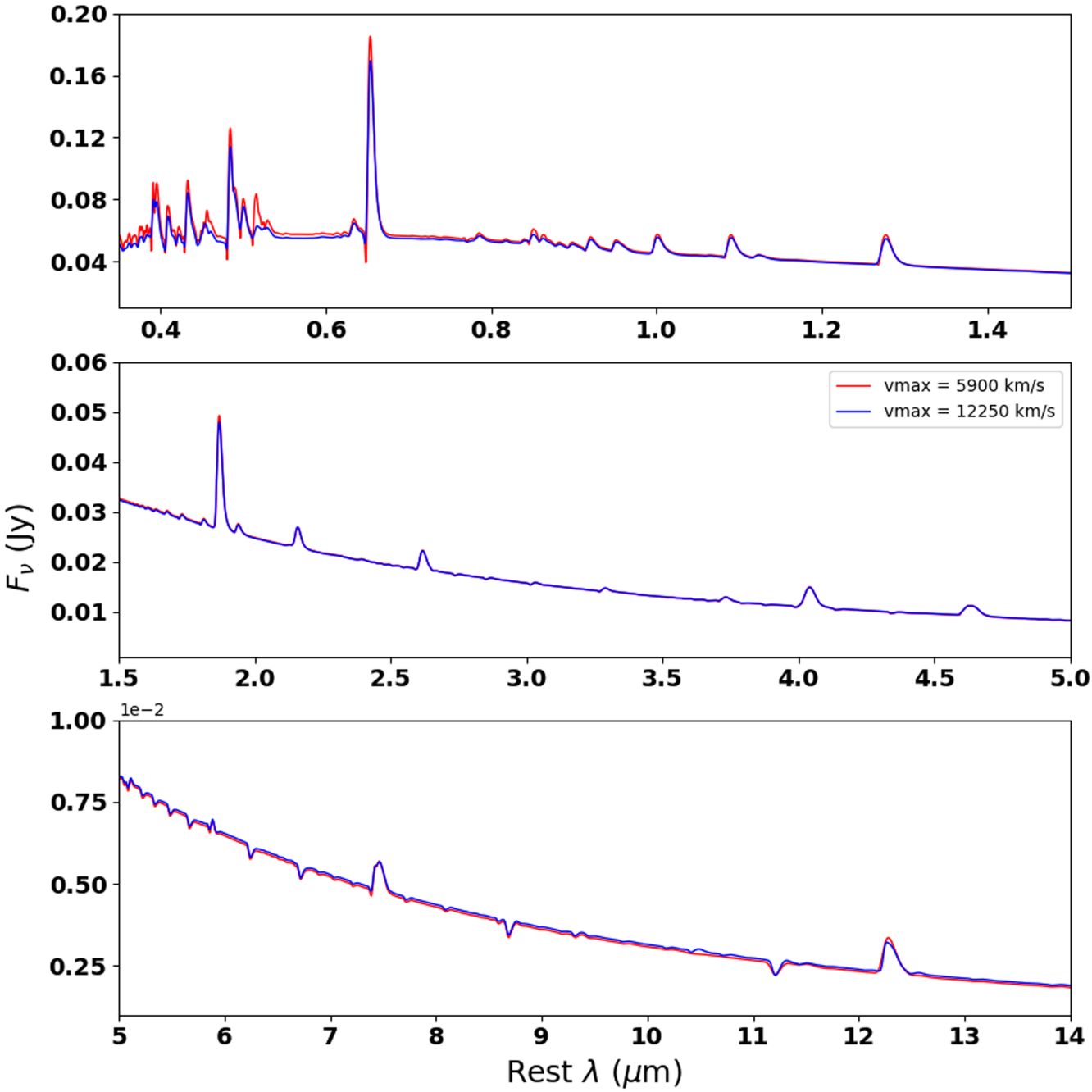

Figure 11. The fiducial model with $v_{\rm max} = 5900$ km s^{-1} and a model with $v_{\rm max} = 12{,}250$ km s^{-1}.

The "bump" on Paγ at $v \sim -1300$ km s^{-1} is interesting; as noted above, it is evident in a few other H I features. If the putative C I line were instead due to the He I 1.083 μm line, it would have a velocity of 7800 km s^{-1}, and it would be difficult to reproduce the P-Cygni shape of the feature since the emission peak of He I would be blended with the emission peak of Paγ, whereas the C I line has an emission peak at its rest wavelength, giving us confidence in the identification. Nevertheless, the Paγ feature could be a blend of Paγ and He I that can only be disentangled by detailed modeling. In a study of 30 SNe II, observed in the NIR, S. Davis et al. (2019) identify the emission component of Paγ feature at 50 days as due to H I, He I, and the Sr II 1.092 μm line, with the absorption primarily due to He I 1.083 μm. Our model, as shown in Figures 7 and 8, finds that the observed feature is due primarily to Paγ in both the emission and absorption components of the P-Cygni feature, and at least in our model, there is no strong evidence for the He I 1.083 μm line. However, Figure 7 clearly shows that there is an additional emission component that is not due to either H I or He I. We explored the possibility that the emission in the model was due to Sr II but found no evidence to support that. We determined that the model feature is due to the Mg II 1.0926 μm transition (see Figure 13). Indeed, Figure 13 shows significant model contributions from Mg II at 0.36376, 0.35521, 0.4432, 0.77899, 0.82316, and 0.9226 μm transitions in addition to the 1.0926 μm transition. Although the model attributes the feature to Mg II, a small bump also appears in the observed spectrum at the same velocity in several other H I features. This suggests that the observed line profiles might be partially influenced by another

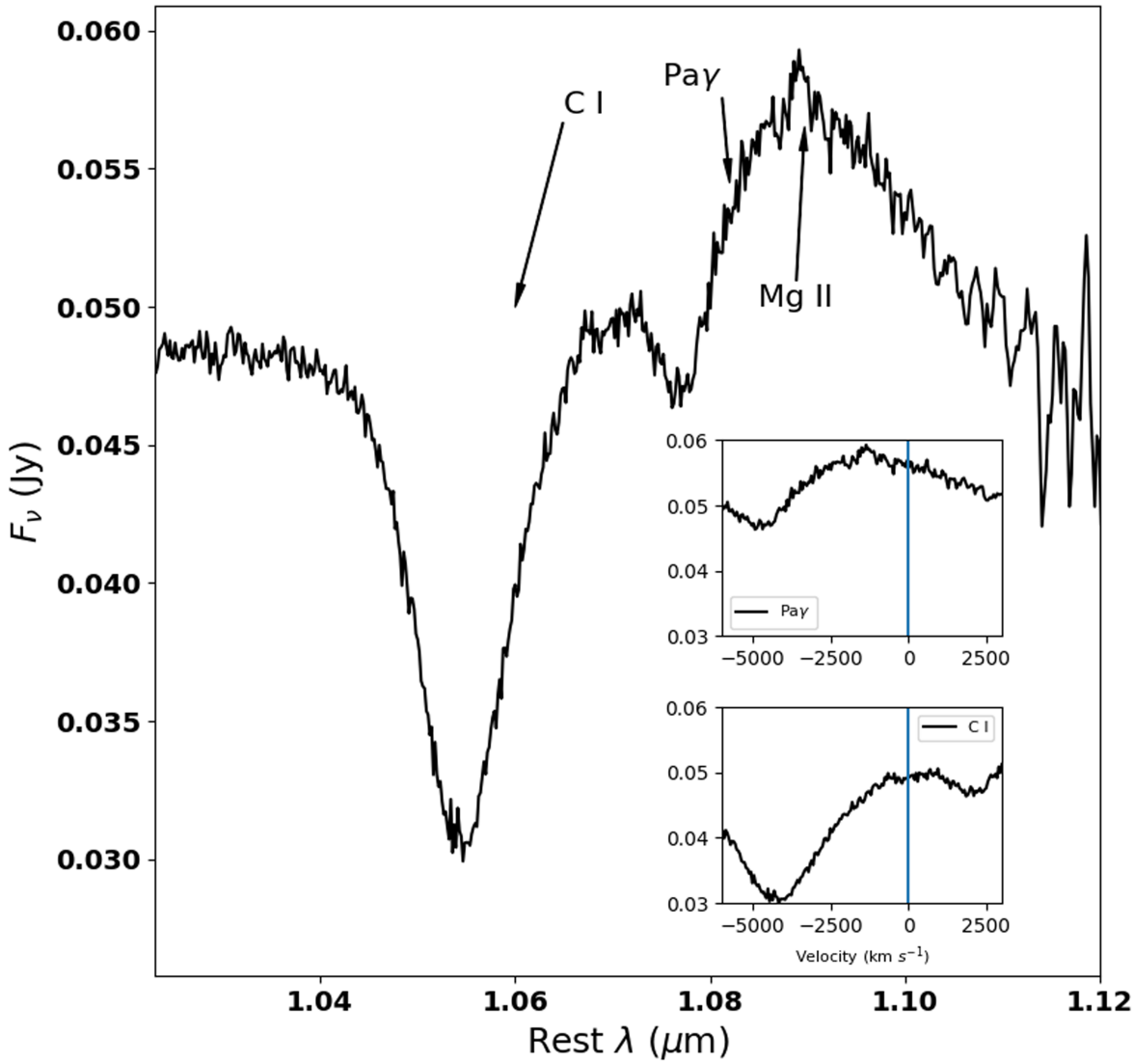

Figure 12. A close-up of the P-Cygni features formed by Paγ and the C I 1.069 μm line (from the IRTF spectrum). Also indicated is the feature on the maximum of Paγ that is almost certainly due to the Mg II 1.0926 μm line (see Section 5). The insets show the velocity extent of the two P-Cygni lines.

effect. These results also show that SN 2024ggi would fall into the weak SN II class of S. Davis et al. (2019). However, S. Davis et al. (2019) find that weak SNe show an absorption feature that they ascribe to high-velocity He I. Since we see no strong evidence for the He I 1.083 μm feature at this epoch, SN 2024ggi does not fit well into either of their classes.

The simple, untuned model does a relatively good job of fitting the strength and width of the lines, suggesting that most of the ejecta is reasonably well described by a power-law density profile, solar compositions, and a velocity extent $v_{\rm max} \lesssim 10{,}000\,{\rm km\,s^{-1}}$. This result is compatible with the value obtained by J. Zhang et al. (2024).

5.0.1. Ca–O

Our model does a poor job on the Ca IR triplet, producing a feature that is too weak and whose blueshifted absorption is too slow, likely because the line is just too weak in the model. However, the model does reproduce the observed separation between the triplet components. It appears likely that, rather than the IR triplet being due to unresolved photospheric and high-velocity components $v_{\rm ph} = 2100$ and $v_{\rm HV} = 7200\,{\rm km\,s^{-1}}$, the 8662 and 8498 components produce separate P-Cygni features with $v = 4900$ and $4400\,{\rm km\,s^{-1}}$, respectively. Even though this is not reproduced by our model (possibly due to clumping, J. Zhang et al. 2024), the velocity extent is reasonably well captured by our model. Our model also does not reproduce the O I 7773.4 Å line; again, the line in the model is much weaker than in the observed spectrum. The model also fails to reproduce the Ca II lines that appear in the two observed spectra as two features that evolve with time.

Since the steep power-law density captures neither the extended velocity profiles in the optical nor the line blanketing, our low estimate of $E_{\rm ejecta} \sim 0.5$ foe is likely a lower limit to the true value of $E_{\rm ejecta}$.

6. Conclusions

We present optical-to-MIR observations of SN 2024ggi obtained on the plateau at ∼55 days after first light. We produce a panchromatic SED from 0.32 to 21 μm. Our data set includes ground-based optical and NIR spectra as well as both JWST NIRSpec and MIRI spectra and imaging. SN 2024ggi was the third SN II to be observed by JWST in the plateau

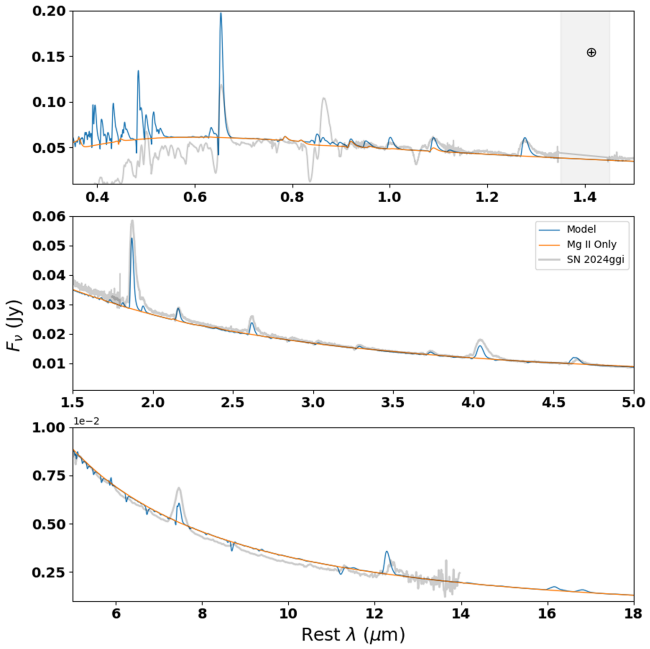

Figure 13. Same as Figure 7 but with all the line opacity except for that due to Mg II turned off.

phase after SN 2022acko and SN 2023ixf. The spectra of SN 2024ggi are consistent with a H recombination spectrum, where the features are primarily produced by H I lines. The NIR+MIR spectral features are broader and have higher velocities compared to the underluminous SN 2022acko. This is consistent with SN 2024ggi being a luminous SN II, likely with a more massive progenitor.

We present a PHOENIX model that is able to reproduce many of the observed spectral features. The model has a density profile with a power-law index of $n = -13$. The velocity extent of the model is rather narrow: $v_{\rm phot} = 3000\,{\rm km\,s^{-1}}$ and $v_{\rm max} = 5900\,{\rm km\,s^{-1}}$. The main discrepancy of the model occurs in the optical, particularly in the line profiles of Hα, O I λ7773.4, and the Ca IR triplet; however, the inferred velocity of the IR triplet is within that of the fiducial model. Thus, it seems likely that clumping is required, perhaps in a cool dense shell in order to reproduce the Ca IR triplet line profile. While a SYNOW fit of Hα fits the blueshifted absorption, simple PHOENIX/1D models do not. It is beyond the scope of this work to fit the Hα profile with toy PHOENIX/1D models (see Appendix B), but it shows the power of panchromatic studies to validate or falsify detailed hydrodynamical models.

We see no evidence of preexisting molecules (CO or SiO) in the system of SN 2024ggi in these early phases. Furthermore, the PHOENIX/1D model does an excellent job of reproducing the continuum at 21 μm (Figure 6), showing there is no evidence of warm or cold dust or excess flux in the MIR. Data we obtained at a later epoch, particularly SN 2024ggi from our JWST Director's Discretionary (DD) programs DD-6677 and DD-6716 (C. Ashall et al. 2024a, 2024b), show clear evidence for CO emission (T. Evans 2025, in preparation). Future observations by JWST will reveal the formation processes of new molecules and potentially dust in the system, helping us to elucidate the origins of dust in the early Universe.

Overall, the panchromatic optical-to-MIR data sets of SNe II provide a powerful tool to investigate the physics of line formation, molecules, and dust in the ejecta. The close proximity of SN 2024ggi offers a unique opportunity for continued monitoring throughout the lifetime of JWST. Future comparative studies with SN 2023ixf, which also has a direct progenitor detection and JWST data, will enable detailed and novel exploration of dust formation pathways and explosion physics in SNe II in a way not previously possible.

The data is available at MAST: doi:10.17909/50v0-my61.

Acknowledgments

E.B., C.A., J.D., M.S., and P.H. acknowledge support from NASA grants JWST-GO-02114, JWST-GO-02122, JWST-GO-04522, JWST-GO-04217, JWST-GO-04436, JWST-GO-03726, JWST-GO-05057, JWST-GO-05290, JWST-GO-06023, JWST-GO-06677, JWST-GO-06213, JWST-GO-06583. Support for programs #2114, #2122, #3726, #4217, #4436, #4522, #5057, #6023, #6213, #6583, and #6677 were provided by NASA through a grant from the Space Telescope Science Institute, which is operated by the Association of Universities for Research in Astronomy, Inc., under NASA contract NAS 5-03127. A.B., E.B., P.B., and P.H. acknowledge support from NASA grant 80NSSC20K0538. E.B., C.A., and J.D. acknowledge support from HST-AR-17555, Support for Program number 17555 was provided through a grant from the STScI under NASA contract NAS5-26555. J.L. acknowledges support from NSF grant AAG-2206523. L.G. acknowledges financial support from AGAUR, CSIC, MCIN and AEI 10.13039/501100011033 under projects PID2023-151307NB-I00, PIE 20215AT016, CEX2020-001058-M, ILINK23001, COOPB2304, and 2021-SGR-01270. M.D.S. is funded by the Independent Research Fund Denmark (IRFD, grant No. 10.46540/2032-00022B). Some of this material is based upon work supported by the National Science Foundation Graduate Research Fellowship Program under grant Nos. 1842402 and 2236415. Any opinions, findings, conclusions, or recommendations expressed in this material are those of the author(s) and do not necessarily reflect the views of the National Science Foundation. The Shappee group at the University of Hawai'i is supported with funds from NSF (grants AST-2407205) and NASA (grants HST-GO-17087, 80NSSC24K0521, 80NSSC24K0490, 80NSSC23K1431). Some of the calculations presented here were performed at the National Energy Research Supercomputer Center (NERSC), which is supported by the Office of Science of the U.S. Department of Energy under Contract No. DE-AC03-76SF00098. The authors gratefully acknowledge the computing time made available to them on the high-performance computers HLRN-IV at GWDG at the NHR Center NHR@Göttingen and at ZIB at the NHR Center NHR@Berlin. These Centers are jointly supported by the Federal Ministry of Education and Research and the state governments participating in the NHR (https://www.nhr-verein.de/unsere-partner). We also thank OU Supercomputing Center for Education & Research (OSCER) at the University of Oklahoma (OU). The Infrared Telescope Facility is operated by the University of Hawaii under contract 80HQTR24DA010 with the National Aeronautics and Space Administration.

Appendix A
Log of JWST Spectral Observations

Table A1 shows the log of the JWST spectral observations.

Table A1
Log of the JWST Spectral Observations

Parameter	Value
NIRSpec Spectral Observations	
Mode	Fixed Slit
T_{obs} (MJD)	60466.465/60466.460
Phase (days)	55.52
Slit	S400A1
Subarray	SUBS400A1
Grating-Filter	G235M-F170LP/G395M-F290LP
Exp Time (s)	60.82/98.22
Groups per Integration	12/20
Integrations per Exp.	1/1
Total Dithers	3/3
Total Integrations	3/3
Readout Pattern	NRS
MIRI Spectral Observations	
Mode	LRS
T_{obs} (MJD)	60466.439
Phase (days)	55.50
Groups per Integration	15
Integrations per Exp.	3
Exposures per Dither	1
Total Dithers	2
Total Exp Time (s)	260.85

Appendix B
Hα Line Profile

In order to probe the results found with the SYNOW fit to Hα a bit further, we ran a few PHOENIX/1D models in LTE, not forcing convergence to radiative equilibrium. The point is just to illustrate the effects of the density profile on the velocity extent of the lines, not to produce a model that fits every feature from the optical to the MIR. The model parameters for the test models (1–3) and the fiducial model are given in Table B1. Figure B1 shows the line profiles of Hα, the Ca IR triplet, Paα, and Pfα for SN 2024ggi for the four models described in Table B1. None of the models does a great job of fitting the blueshifted absorption trough of Hα; Model 1 with the density profile inferred from the SYNOW calculation extends way too far to the blue, whereas the steeper-density profiles in Models 2 and 3 do a somewhat better job of reproducing the observed velocity extent. Only the fiducial model does a good job of reproducing the shape of the rest wavelength Hα emission peak. Moving to the Ca IR triplet, all of the LTE models produce blueshifted absorption troughs that extend too far to the blue and show no separation among the components of the triplet, whereas that is evident in the data. The steeper-density Models 2 and 3 do a reasonable job of replicating the rest wavelength emission peak of the P-Cygni profile, while the fiducial model shows only a very weak Ca IR triplet. Moving to the NIR and MIR, the fiducial model does a much better job of reproducing both Paα and Pfα.

Table B1
Parameters of the Comparison PHOENIX/1D Models

Model	NLTE	Density Profile	v_0 (km s^{-1})	v_e (km s^{-1})	v_{max} (km s^{-1})
Fiducial	Yes	$(v/v_0)^{-13}$	3000	⋯	5900
1	No	$\exp[-(v - v_0)/v_e]$	3500	2000	13000
2	No	$\exp[-(v - v_0)/v_e]$	3500	800	9800
3	No	$\exp[-(v - v_0)/v_e]$	3500	800	13500

While it is beyond the scope of this work to attempt to find "the model" of SN 2024ggi, it is clear that the fiducial model captures much of the line and continuum formation in the NIR and MIR but that there is more complexity needed to reproduce the optical features. This work does show the power of long multiwavelength spectroscopy and photometry to produce data that can validate or falsify detailed models.

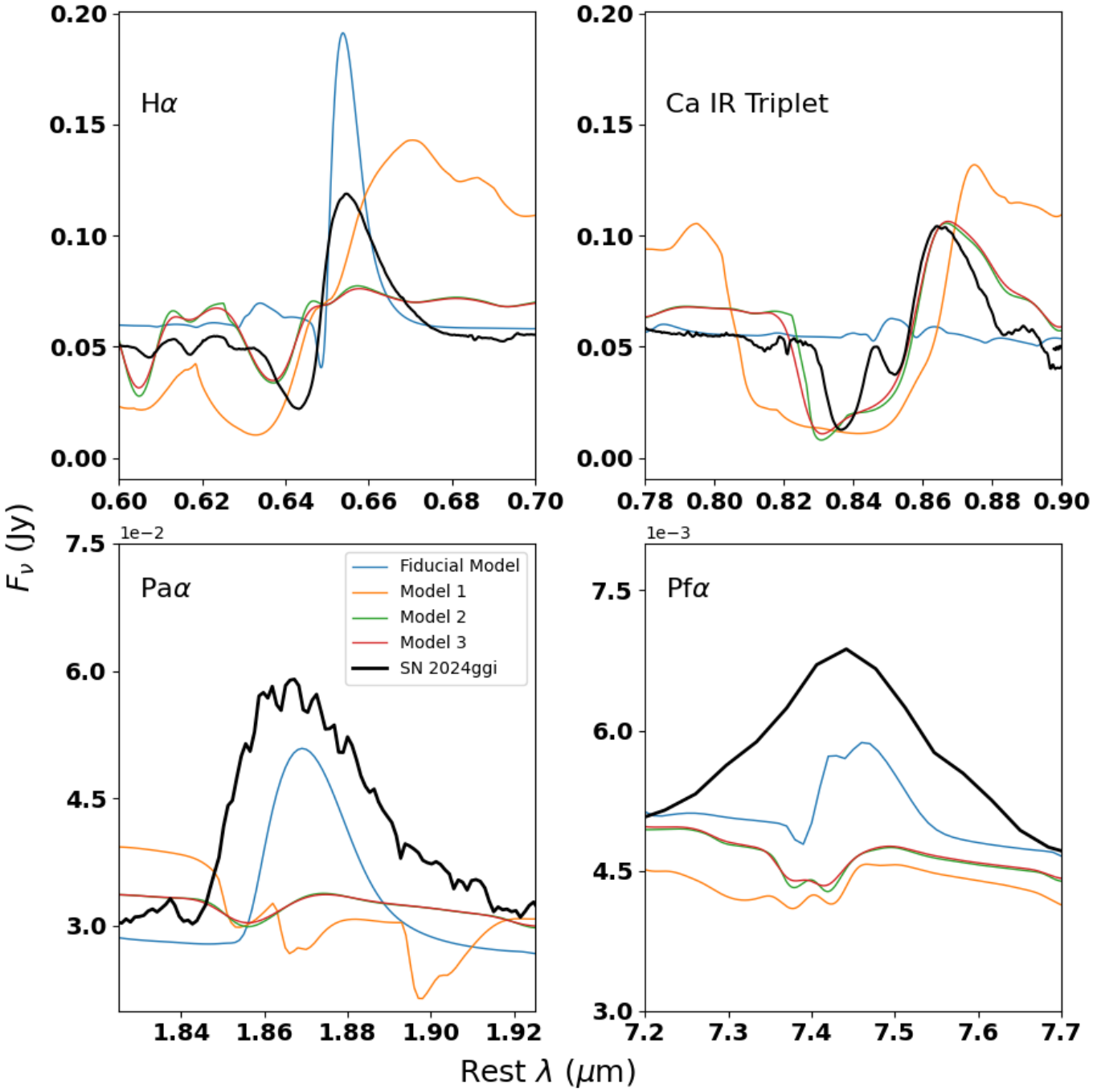

Figure B1. The line profiles of Hα (upper left panel), Ca IR triplet (upper right panel), Paα (lower left panel), and Pfα (lower right panel). Models with more extended velocity profiles capture the velocity extent of the optical features but do a poorer job of reproducing the shape of the NIR and MIR features. The synthetic spectra have been scaled for clarity. See Appendix B for more details.

ORCID iDs

E. Baron https://orcid.org/0000-0001-5393-1608
C. Ashall https://orcid.org/0000-0002-5221-7557
J. M. DerKacy https://orcid.org/0000-0002-7566-6080
P. Hoeflich https://orcid.org/0000-0002-4338-6586
K. Medler https://orcid.org/0000-0001-7186-105X
M. Shahbandeh https://orcid.org/0000-0002-9301-5302
E. Fereidouni https://orcid.org/0009-0001-9148-8421
C. M. Pfeffer https://orcid.org/0000-0002-7305-8321
T. Mera https://orcid.org/0000-0001-5888-2542
W. B. Hoogendam https://orcid.org/0000-0003-3953-9532
S. Shiber https://orcid.org/0000-0001-6107-0887
K. Auchettl https://orcid.org/0000-0002-4449-9152
P. J. Brown https://orcid.org/0000-0001-6272-5507
C. R. Burns https://orcid.org/0000-0003-4625-6629
A. Burrow https://orcid.org/0000-0002-5380-0816
D. A. Coulter https://orcid.org/0000-0003-4263-2228
M. Engesser https://orcid.org/0000-0003-0209-674X
G. Folatelli https://orcid.org/0000-0001-5247-1486
O. Fox https://orcid.org/0000-0003-2238-1572
L. Galbany https://orcid.org/0000-0002-1296-6887
M. Guolo https://orcid.org/0000-0002-5063-0751
J. T. Hinkle https://orcid.org/0000-0001-9668-2920

Mark E. Huber https://orcid.org/0000-0003-1059-9603
E. Y. Hsiao https://orcid.org/0000-0003-1039-2928
T. de Jaeger https://orcid.org/0000-0001-6069-1139
D. O. Jones https://orcid.org/0000-0002-6230-0151
S. Kumar https://orcid.org/0000-0001-8367-7591
J. Lu https://orcid.org/0000-0002-3900-1452
P. A. Mazzali https://orcid.org/0000-0001-6876-8284
N. Morrell https://orcid.org/0000-0003-2535-3091
M. M. Phillips https://orcid.org/0000-0003-2734-0796
A. Rest https://orcid.org/0000-0002-4410-5387
N. B. Suntzeff https://orcid.org/0000-0002-8102-181X
B. J. Shappee https://orcid.org/0000-0003-4631-1149
Jennifer Shi https://orcid.org/0009-0008-3724-1824
M. D. Stritzinger https://orcid.org/0000-0002-5571-1833
L. Strolger https://orcid.org/0000-0002-7756-4440
T. Temim https://orcid.org/0000-0001-7380-3144
S. Tinyanont https://orcid.org/0000-0002-1481-4676
M. Tucker https://orcid.org/0000-0002-2471-8442
L. Wang https://orcid.org/0000-0001-7092-9374
Q. Wang https://orcid.org/0000-0001-5233-6989
Y. Yang https://orcid.org/0000-0002-6535-8500

References

Aitken, D. K., Smith, C. H., James, S. D., et al. 1988, MNRAS, 231, 7P
Arnett, W. D., Bahcall, J. N., Kirshner, R. P., & Woosley, S. E. 1989, ARA&A, 27, 629
Ashall, C., Baron, E., DerKacy, J. M., et al. 2024a, JWST Proposal 6677
Ashall, C., Baron, E., DerKacy, J. M., et al. 2024b, JWST Proposal 6716
Asplund, M., Grevesse, N., Sauval, A. J., & Scott, P. 2009, ARA&A, 47, 481
Baron, E., Bongard, S., Branch, D., & Hauschildt, P. H. 2006, ApJ, 645, 480
Baron, E., Branch, D., Hauschildt, P. H., Filippenko, A. V., & Kirshner, R. P. 1999, ApJ, 527, 739
Baron, E., Branch, D., Hauschildt, P. H., et al. 2000, ApJ, 545, 444
Baron, E., Hauschildt, P. H., Branch, D., et al. 1993, ApJL, 416, L21
Baron, E., Hauschildt, P. H., Branch, D., et al. 1995, ApJ, 441, 170
Baron, E., Hauschildt, P. H., Nugent, P., & Branch, D. 1996, MNRAS, 283, 297
Baron, E., Jeffery, D. J., Branch, D., et al. 2008, ApJ, 672, 1038
Baron, E., Nugent, P. E., Branch, D., & Hauschildt, P. H. 2004, ApJL, 616, L91
Baron, E., Nugent, P. E., Branch, D., et al. 2003, ApJ, 586, 1199
Benetti, S., Turatto, M., Balberg, S., et al. 2001, MNRAS, 322, 361
Bongard, S., Baron, E., Smadja, G., Branch, D., & Hauschildt, P. H. 2006, ApJ, 647, 513
Bongard, S., Baron, E., Smadja, G., Branch, D., & Hauschildt, P. H. 2008, ApJ, 687, 456
Bostroem, K. A., Dessart, L., Hillier, D. J., et al. 2023, ApJL, 953, L18
Bostroem, K. A., Valenti, S., Horesh, A., et al. 2019, MNRAS, 485, 5120
Bouchet, P., Phillips, M. M., Suntzeff, N. B., et al. 1991, A&A, 245, 490
Bouchet, P., Stanga, R., Moneti, A., et al. 1987, in European Southern Observatory Conf. and Workshop Proc. 26, ed. I. J. Danziger (Garching: ESO), 159
Branch, D. 1980, in AIP Conf. Ser. 63, Supernovae Spectra, ed. R. Meyerott & H. G. Gillespie (Melville, NY: AIP), 39
Branch, D., Baron, E., Hall, N., Melakayil, M., & Parrent, J. 2005, PASP, 117, 545
Branch, D., Dang, L. C., Hall, N., et al. 2006, PASP, 118, 560
Branch, D., Garnavich, P., Matheson, T., et al. 2003, AJ, 126, 1489
Brown, G. E. 2005, PhT, 58, 62
Catchpole, R. M., Whitelock, P. A., Feast, M. W., et al. 1988, MNRAS, 231, 75P
Catchpole, R. M., Whitelock, P. A., Menzies, J. W., et al. 1989, MNRAS, 237, 55P
Chambers, K. C., Boer, T. D., Herman, J., et al. 2024, TNSTR 2024-1116, 1
Chen, T.-W., Yang, S., Srivastav, S., et al. 2025, ApJ, 983, 86
Chen, X., Kumar, B., Er, X., et al. 2024, ApJL, 971, L2
Dall'Ora, M., Botticella, M. T., Pumo, M. L., et al. 2014, ApJ, 787, 139
Danziger, I. J., Lucy, L. B., Bouchet, P., & Gouiffes, C. 1991, in 10th Santa Cruz Workshop in Astronomy and Astrophysics, Supernovae, ed. S. E. Woosley (New York: Springer), 69
Davis, S., Hsiao, E. Y., Ashall, C., et al. 2019, ApJ, 887, 4
de Jaeger, T., Galbany, L., González-Gaitán, S., et al. 2020, MNRAS, 495, 4860
DerKacy, J. M., Ashall, C., Baron, E., et al. 2025, arXiv:2507.18785
DerKacy, J. M., Baron, E., Branch, D., et al. 2020, ApJ, 901, 86
Dessart, L., & Hillier, D. J. 2005, A&A, 437, 667
Eastman, R. G., & Kirshner, R. P. 1989, ApJ, 347, 771
Elias, J. H., Gregory, B., Phillips, M. M., et al. 1988, ApJL, 331, L9
Elmhamdi, A., Danziger, I. J., Chugai, N., et al. 2003, MNRAS, 338, 939
Ertini, K., Regna, T. A., Ferrari, L., et al. 2025, A&A, 699, A60
Fox, O. D., Chevalier, R. A., Skrutskie, M. F., et al. 2011, ApJ, 741, 7
Fraser, M., Ergon, M., Eldridge, J. J., et al. 2011, MNRAS, 417, 1417
Friesen, B., Baron, E., Parrent, J. T., et al. 2017, MNRAS, 467, 2392
Hamuy, M., & Pinto, P. A. 2002, ApJL, 566, L63
Hamuy, M., Pinto, P. A., Maza, J., et al. 2001, ApJ, 558, 615
Harkness, R. P., & Wheeler, J. C. 1988, PASA, 7, 431
Hauschildt, P. H., & Baron, E. 1999, JCoAM, 109, 41
Hauschildt, P. H., & Ensman, L. M. 1994, ApJ, 424, 905
Hillier, D. J., & Miller, D. L. 1998, ApJ, 496, 407
Hinds, K. R., Perley, D. A., Sollerman, J., et al. 2025, MNRAS, 541, 135
Hoeflich, P. 1988, PASA, 7, 434
Hong, X., Sun, N.-C., Niu, Z., et al. 2024, ApJL, 977, L50
Hoogendam, W., Auchettl, K., Tucker, M., et al. 2024, TNSAN 2024-103, 1
Hoogendam, W. B., Ashall, C., Jones, D. O., et al. 2025a, ApJ, 988, 209
Hoogendam, W. B., Jones, D. O., Ashall, C., et al. 2025b, OJAp, 8, 120
Hsiao, E. Y., Phillips, M. M., Marion, G. H., et al. 2019, PASP, 131, 014002
Hu, M., Ao, Y., Yang, Y., et al. 2025, ApJL, 978, L27
Jacobson-Galán, W. V., Davis, K. W., Kilpatrick, C. D., et al. 2024, ApJ, 972, 177
Janka, H.-T. 2025, ARNPS, 75, 425
Jeffery, D. J., & Branch, D. 1990, in Jerusalem Winter School for Theoretical Physics, Supernovae, 6, ed. J. C. Wheeler, T. Piran, & S. Weinberg (Singapore: World Scientific), 149
Jerkstrand, A., Fransson, C., & Kozma, C. 2011, A&A, 530, A45
Jerkstrand, A., Smartt, S. J., Fraser, M., et al. 2014, MNRAS, 439, 3694
Jones, O. C., Kavanagh, P. J., Barlow, M. J., et al. 2023, ApJ, 958, 95
Kasen, D., Thomas, R. C., & Nugent, P. 2006, ApJ, 651, 366
Kerzendorf, W. E., & Sim, S. A. 2014, MNRAS, 440, 387
Kotak, R., Meikle, P., Pozzo, M., et al. 2006, ApJL, 651, L117
Kotak, R., Meikle, W. P. S., Farrah, D., et al. 2009, ApJ, 704, 306
Kozma, C., & Fransson, C. 1998, ApJ, 497, 431
Kromer, M., & Sim, S. A. 2009, MNRAS, 398, 1809
Lantz, B., Aldering, G., Antilogus, P., et al. 2004, Proc. SPIE, 5249, 146
Larsson, J., Fransson, C., Sargent, B., et al. 2023, ApJL, 949, L27
Lee, J. C., Whitmore, B. C., Thilker, D. A., et al. 2022, ApJS, 258, 10
Lentz, E. J., Baron, E., Branch, D., & Hauschildt, P. H. 2001a, ApJ, 547, 402
Lentz, E. J., Baron, E., Branch, D., & Hauschildt, P. H. 2001b, ApJ, 557, 266
Lentz, E. J., Baron, E., Lundqvist, P., et al. 2001c, ApJ, 547, 406
Leroy, A., Kreckel, K., Lee, J., et al. 2023, JWST Proposal 3707
Lucy, L. B. 1988, in Supernova 1987A in the Large Magellanic Cloud, ed. M. Kafatos & A. G. Michalitsianos (Cambridge: Cambridge Univ. Press), 323
Maguire, K., Di Carlo, E., Smartt, S. J., et al. 2010, MNRAS, 404, 981
Mazzali, P. A., Lucy, L. B., & Butler, K. 1992, A&A, 258, 399
Medler, K., Ashall, C., Hoeflich, P., et al. 2025a, ApJ, 993, 191
Medler, K., Ashall, C., Shahbandeh, M., et al. 2025b, ApJS, 281, 28
Meikle, W. P. S., Allen, D. A., Spyromilio, J., & Varani, G. F. 1989, MNRAS, 238, 193
Meikle, W. P. S., Cumming, R. J., Spyromilio, J., Allen, D. A., & Mobasher, B. 1991, in European Southern Observatory Conf. and Workshop Proc. 37, Supernova 1987A and Other Supernovae, ed. I. J. Danziger & K. Kjaer (Garching: ESO), 595
Meikle, W. P. S., Spyromilio, J., Allen, D. A., Varani, G. F., & Cumming, R. J. 1993, MNRAS, 261, 535
Mitchell, R. C., Baron, E., Branch, D., et al. 2002, ApJ, 574, 293
Morokuma, T., Tominaga, N., Tanaka, M., et al. 2014, PASJ, 66, 114
Nugent, P., Phillips, M., Baron, E., Branch, D., & Hauschildt, P. 1995, ApJL, 455, L147
Oliva, E., Moorwood, A. F. M., & Danziger, I. J. 1987, Msngr, 50, 18
Pastorello, A., Valenti, S., Zampieri, L., et al. 2009, MNRAS, 394, 2266
Payne-Gaposchkin, C., & Whipple, F. L. 1940, PNAS, 26, 264
Perrin, M. D., Sivaramakrishnan, A., Lajoie, C. P., et al. 2014, Proc. SPIE, 9143, 91433X
Pessi, T., Cartier, R., Hueichapan, E., et al. 2024, A&A, 688, L28
Phillips, M. M., Contreras, C., Hsiao, E. Y., et al. 2019, PASP, 131, 014001
Phillips, M. M., Simon, J. D., Morrell, N., et al. 2013, ApJ, 779, 38

Poznanski, D., Prochaska, J. X., & Bloom, J. S. 2012, MNRAS, 426, 1465
Pozzo, M., Meikle, W. P. S., Rayner, J. T., et al. 2006, MNRAS, 368, 1169
Rank, D. M., Bregman, J., Witteborn, F. C., et al. 1988, ApJL, 325, L1
Rho, J., Geballe, T. R., Banerjee, D. P. K., et al. 2018, ApJL, 864, L20
Saha, A., Thim, F., Tammann, G. A., Reindl, B., & Sandage, A. 2006, ApJS, 165, 108
Schlafly, E. F., & Finkbeiner, D. P. 2011, ApJ, 737, 103
Shahbandeh, M., Ashall, C., Hoeflich, P., et al. 2024, arXiv:2401.14474
Sharp, C. M., & Hoeflich, P. 1990, Ap&SS, 171, 213
Shrestha, M., Bostroem, K. A., Sand, D. J., et al. 2024, ApJL, 972, L15
Sim, S. A. 2007, MNRAS, 375, 154
Singh, A., Teja, R. S., Moriya, T. J., et al. 2024, ApJ, 975, 132
Smith, N. 2017, in Handbook of Supernovae, ed. A. W. Alsabti & P. Murdin (Berlin: Springer), 403
Soker, N. 2024, OJAp, 7, 69
Spyromilio, J., Leibundgut, B., & Gilmozzi, R. 2001, A&A, 376, 188
Spyromilio, J., Meikle, W. P. S., Learner, R. C. M., & Allen, D. A. 1988, Natur, 334, 327
Srivastav, S., Chen, T. W., Smartt, S. J., et al. 2024, TNSAN 2024-100, 1
Swartz, D. A., Harkness, R. P., & Wheeler, J. C. 1989, Natur, 337, 439
Szalai, T., & Vinkó, J. 2013, A&A, 549, A79
Szalai, T., Zsíros, S., Fox, O. D., Pejcha, O., & Müller, T. 2019, ApJS, 241, 38
Takáts, K., Pignata, G., Pumo, M. L., et al. 2015, MNRAS, 450, 3137
Takáts, K., Pumo, M. L., Elias-Rosa, N., et al. 2014, MNRAS, 438, 368
Tomasella, L., Cappellaro, E., Fraser, M., et al. 2013, MNRAS, 434, 1636
Tonry, J., Denneau, L., Weiland, H., et al. 2024, TNSTR 2024-0201, 1
Tucker, M. A., Hinkle, J., Angus, C. R., et al. 2024, ApJ, 976, 178
Tucker, M. A., Shappee, B. J., Huber, M. E., et al. 2022, PASP, 134, 124502
Valenti, S., Howell, D. A., Stritzinger, M. D., et al. 2016, MNRAS, 459, 3939
Valenti, S., Sand, D., Stritzinger, M., et al. 2015, MNRAS, 448, 2608
Vartanyan, D., Tsang, B. T. H., Kasen, D., et al. 2025, ApJ, 982, 9
Whitelock, P. A., Catchpole, R. M., Menzies, J. W., et al. 1988, MNRAS, 234, 5P
Wooden, D. H., Rank, D. M., Bregman, J. D., et al. 1993, ApJS, 88, 477
Xiang, D., Mo, J., Wang, X., et al. 2024, ApJL, 969, L15
Zhai, Q., Li, L., Wang, Z., Zhang, J., & Wang, X. 2024, TNSAN 2024-104, 1
Zhang, J., Dessart, L., Wang, X., et al. 2024, ApJL, 970, L18
Zheng, W., Dessart, L., Filippenko, A. V., et al. 2025, ApJ, 988, 61